

RESEARCH ARTICLE

Unified one-fluid formulation for incompressible flexible solids and multiphase flows: Application to hydrodynamics using the immersed structural potential method (ISPM)

Liang Yang^{1,3}  | Antonio J. Gil¹  | Aurelio Arranz Carreño¹ | Javier Bonet²

¹Zienkiewicz Centre for Computational Engineering, College of Engineering, Swansea University, Bay Campus, SA1 8EN, UK

²University of Greenwich, London, SE10 9LS, UK

³Department of Earth Science & Engineering, Imperial College London, South Kensington Campus, SW7 2AZ, UK

Correspondence

Antonio J. Gil, Zienkiewicz Centre for Computational Engineering, College of Engineering, Swansea University, Bay Campus, SA1 8EN, UK.
Email: a.j.gil@swansea.ac.uk

Summary

In this paper, we present a two-dimensional computational framework for the simulation of fluid-structure interaction problems involving incompressible flexible solids and multiphase flows, further extending the application range of classical immersed computational approaches to the context of hydrodynamics. The proposed method aims to overcome shortcomings such as the restriction of having to deal with similar density ratios among different phases or the restriction to solve single-phase flows. First, a variation of classical immersed techniques, pioneered with the immersed boundary method (IBM), is presented by rearranging the governing equations, which define the behaviour of the multiple physics involved. The formulation is compatible with the “one-fluid” formulation for two-phase flows and can deal with large density ratios with the help of an anisotropic Poisson solver. Second, immersed deformable structures and fluid phases are modelled in an identical manner except for the computation of the deviatoric stresses. The numerical technique followed in this paper builds upon the immersed structural potential method developed by the authors, by adding a level set-based method for the capturing of the fluid-fluid interfaces and an interface Lagrangian-based meshless technique for the tracking of the fluid-structure interface. The spatial discretisation is based on the standard marker-and-cell method used in conjunction with a fractional step approach for the pressure/velocity decoupling, a second-order time integrator, and a fixed-point iterative scheme. The paper presents a wide range of two-dimensional applications involving multiphase flows interacting with immersed deformable solids, including benchmarking against both experimental and alternative numerical schemes.

KEYWORDS

fluid-structure interaction, hydrodynamics, ISPM, immersed boundary, level sets, unified one-fluid formulation

1 | INTRODUCTION

Within the field of computational fluid-structure interaction (FSI), two families of methodologies can be clearly identified, namely, body-fitted methods¹⁻⁵ and immersed methods.⁶⁻¹⁶ Schemes and algorithms within each family have some strengths and weaknesses, which have been well documented over the years. Within the group of body-fitted methodologies,

the main disadvantage is the computational cost related to the update of the mesh and the possible need to resort to remeshing algorithms. Immersed methods have recently gained popularity as they help to address this specific shortcoming; however, they can suffer from numerically sub-optimality in the region around the interface (see Gil et al,¹⁶ page 8628, figures 9 and 10, for numerical evidence). Specifically, the use of a single polynomial interpolating function to describe the velocity field across the interface can only render suboptimal results. Moreover, the continuous nature of the pressure approximation across the interface can also compromise global mass conservation. Traditionally, authors tend to alleviate this shortcoming by resorting to fine discretisations near the interface. An alternative recent trend to completely overcome these consistency issue is the combination of a local XFEM enrichment with a cut-finite element method (FEM) methodology and a Lagrange multiplier (or a Nitsche's method) treatment of the interface coupling.¹⁷⁻¹⁹

The pioneering IBM was first introduced by Peskin⁶ to simulate the deformation of heart valves. The distinguishing feature of this method is the fact that the simulation is carried out on a fixed Eulerian Cartesian grid, which does not conform to that of the current geometry of the deformed immersed structure. A solid-to-fluid interpolated body force is added to the fluid to account for the presence of any immersed deformable solid. Early versions of the IBM were limited to the case of immersed solids made up of fibres satisfying the generalised Hooke's law.^{7-9,20} The original method was defined on the basis of the finite difference method, and an approximation of the Dirac delta distribution was used to map information (ie, velocity and forces) between the Eulerian fluid and the Lagrangian immersed solid.²¹ The material properties of the immersed continuum have been recently extended to those of a viscoelastic structure²² or even to those of a fluid²³ or a dry foam.²⁴ Furthermore, adaptive remeshing techniques²⁵ were also introduced to improve the accuracy of the technique in the vicinity of the interface between the different physics involved in the problem.

Because of a considerable revival of the IBM, the methodology is no longer restricted to modelling simplified fibre-like solids. More realistic continuum-like structures can also be analysed because of enhancements introduced on the original methodology, which have led to alternative approaches, such as the extended immersed boundary method originally presented by Wang and Liu²⁶ and the immersed finite element method (IFEM) pioneered by Zhang et al²⁷ and fully exploited by Liu et al.¹¹ In this approach, the immersed structure is modelled by means of the FEM, where standard piecewise polynomial shape functions are used to compute the deformation gradient tensor \mathbf{F} within the immersed structure domain. The nodal displacement field of the immersed finite element mesh is computed after time integration of the nodal velocity field, which is obtained after suitable interpolation of the velocity field from the background fluid domain with the help of interpolation functions defined on the fluid. The force field at the nodes of the deformable solid finite element mesh is computed as a result of the spatial integration of the stress tensor through the use of the spatial gradient of standard nodal finite element shape functions.

Gil et al¹⁶ introduced the immersed structural potential method (ISPM) for the solution of single-phase FSI problems interacting with highly deformable structures in the context of haemodynamic applications (ie, low density ratios). This methodology is in line with but distinct from approaches such as the material point method²⁸ or the force-projection method presented by Zhao et al.²⁹ The immersed structure is generalised to any continuum described by means of a deviatoric strain energy functional, as in the work of Devendran and Peskin.²² From the spatial discretisation point of view, the structure is modelled as a collection of integration points, which deform according to the kinematics defined by the background fluid. Tailor-made kernel functions¹³ were designed to compute the velocity field and the spatial gradient velocity tensor \mathbf{l} directly at an integration point level. A structure preserving time-integration scheme is then used to compute the deformation gradient tensor \mathbf{F} at every integration point, yielding improved accuracy and stability over previous immersed-based methodologies.¹³ The update of \mathbf{F} from \mathbf{l} prevents the appearance of locking, which is a problem often encountered when using low-order approximations (see Hesch et al,¹⁴ Section 5.3, page 62, for numerical evidence). A similar methodology in the context of fast solid dynamics has been used by the authors.³⁰⁻³⁶

For the simulation of multiphase flows, some authors have opted for the Lagrangian smoothed particle hydrodynamics (SPH) method³⁷ and others for the Eulerian "one-fluid" formulation.³⁸ The latter approach is followed in this paper, where the computational modelling is performed in a similar way to that of a single-phase flow, apart from the treatment of the interface evolution, which is considered dependent on the flow velocity field. There are two possible descriptions of the interface kinematics, namely, the interface can be explicitly "tracked" in a Lagrangian fashion or be "captured" with an implicit marker function. In the case of using an explicit description, a possible way to follow the interface is through a cloud of interpolation points or particles, as in the case of the front tracking method.³⁹⁻⁴¹ On the other hand, the most popular implicit descriptions of the interfaces are established by the volume of fluid method^{42,43} and the level set method.^{44,45}

The solution of problems involving multiphase flows and immersed structures is a complex problem, which still requires further research. Classical immersed computational techniques struggle computationally when having to deal efficiently with problems between phases with large density ratios, as typically encountered in hydrodynamic engineering applications. In this paper, a unified one-fluid formulation will be presented aiming to address this shortcoming. In this work, the level set method is

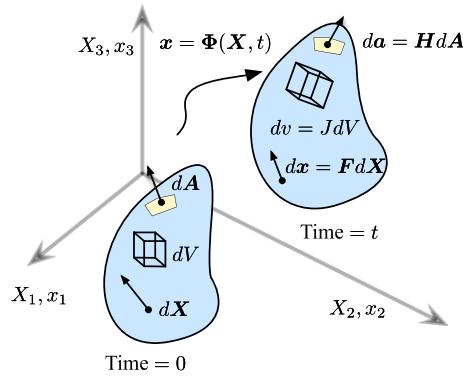


FIGURE 1 The general deformation of a continuum and kinematic strain measure $\{F, H, J\}$ [Colour figure can be viewed at wileyonlinelibrary.com]

favoured to capture the fluid interface, as it presents advantages when dealing with topological changes. Moreover, Lagrangian particles or integration points are used to describe the motion of the immersed flexible body, which facilitates the preservation of mass. It is noteworthy to highlight that a unified Lagrangian formulation has been recently proposed by Franci et al,⁴⁶ where both fluid and solid phases are solved in a similar Lagrangian fashion.

The outline of the paper is as follows. Section 2 introduces the classical Eulerian conservation laws (conservation of linear momentum and conservation of mass) for multiphase continuum by introducing well-known jump conditions. Constitutive models for the various phases in the form of a Newtonian fluid and a hyperelastic deformable solid are also presented. Section 3 presents a unified framework for the computational modelling of the multiphase continuum by making use of a smooth representation of the indicator function. The proposed “one-fluid” model is capable of dealing with multiple fluids as well as structures. In addition, some of the available techniques for the description of interfaces are briefly revisited, namely, an Eulerian (capturing) level set method and a Lagrangian (tracking) particle method. Section 4 discusses the details of the numerical discretisation of the multiphase flow governing equations. An efficient second-order finite volume scheme set in a Cartesian staggered mesh is chosen for the spatial discretisation in conjunction with a well-established fractional step method for the fluid-pressure decoupling. The discrete representation of the deformable immersed solid is performed according with the ISPM, and tension effects are also incorporated. Section 5 presents some hydrodynamics problems, which involve air, water, and immersed structures, illustrating the capability of the proposed method.

2 | GOVERNING EQUATIONS

2.1 | Kinematics of a continuum

Let us consider the motion of a continuum from its undeformed (or material) configuration $\Omega_0 \subset \mathbb{R}^d$ with boundary $\partial\Omega_0$ and outward unit normal N , into its deformed (or spatial) configuration $\Omega_t(t) \subset \mathbb{R}^d$ at time t , with boundary $\partial\Omega_t(t)$ and outward unit normal n , where d represents the number of spatial dimensions ($d = 2$ for the examples included in this paper). The motion is described by a time $t \in [0, T]$ dependent mapping field Φ , which links a material particle from material configuration X to spatial configuration x according to $x(t) = \Phi(X, t)$ (see Figure 1).

The following well-known strain measures can be introduced as follows. The two-point deformation gradient tensor or fibre map F , which relates a fibre of differential length from the material configuration dX to the spatial configuration dx , namely, $dx = FdX$, is defined as the material gradient ∇_0 of the spatial configuration, namely,

$$F = \nabla_0 x = \frac{\partial \Phi(X, t)}{\partial X}. \tag{1}$$

In addition, the Jacobian J or volume map of the deformation relates differential volume elements in the material configuration $d\Omega_0$ and the spatial configuration $d\Omega$ as $d\Omega = Jd\Omega_0$, defined as

$$J = \det F. \tag{2}$$

Finally, and for completeness, the two-point co-factor or adjoint tensor H can be introduced to map the element area vector from material configuration dA (colinear with N) to spatial configuration da (colinear with n) as $da = HdA$, defined as

$$\mathbf{H} = \frac{1}{2} \mathbf{F} \times \mathbf{F}. \quad (3)$$

where use has been made of the cross product between two second-order tensors as presented by Bonet et al.⁴⁷ Apart from the fundamental strain measures $\{\mathbf{F}, \mathbf{H}, \mathbf{J}\}$ introduced above, the velocity field \mathbf{u} of the continuum is defined as the material time derivative of the mapping Φ as $\mathbf{u} = \frac{\partial \Phi(\mathbf{X}, t)}{\partial t}$. Finally, another kinematic entity of interest is the velocity gradient tensor \mathbf{l} , which is defined as the spatial gradient ∇ of the velocity field, namely, $\mathbf{l} = \nabla \mathbf{u}$. As it is well known, the evaluation of \mathbf{l} requires the use of the inverse mapping relationship, that is, $\mathbf{l} = \frac{\partial \mathbf{u}(\Phi^{-1}(\mathbf{x}, t), t)}{\partial \mathbf{x}}$.⁴⁸ This relationship can be alternatively written as

$$\frac{d\mathbf{F}}{dt} = \mathbf{l}\mathbf{F}, \quad (4)$$

which relates the material derivative $\frac{d}{dt}$ of the deformation gradient tensor \mathbf{F} with the velocity gradient tensor \mathbf{l} and \mathbf{F} itself.

In the particular case of an incompressible continuum, the Jacobian of the deformation satisfies $J = 1$ (Lagrangian description) or, alternatively in an Eulerian description,

$$\mathbf{l} : \mathbf{I} = \nabla \cdot \mathbf{u} = 0, \quad (5)$$

where the operator $\nabla \cdot$ represents the spatial divergence and \mathbf{I} is the second-order identity tensor. For the examples presented in this paper, this kinematic constraint will always apply.

In general, the continuum can contain internal interfaces separating different subdomains or phases (ie, fluid-fluid, solid-solid, fluid-solid). In this case, suitable jump conditions can be introduced on every interface. In the special case of nonslip conditions (of interest in this paper) and in the absence of shock waves, the jump conditions for the mapping Φ can be defined (in terms of Φ or in terms of the velocity field \mathbf{u}) as

$$[[\Phi]] = \mathbf{0}; \quad [[\mathbf{u}]] = \mathbf{0}, \quad (6)$$

where the operator $[[\cdot]]$ represents the jump in the variable of interest across the interface. Similar jump conditions can be defined for the strain measures \mathbf{F} and \mathbf{H} , but will not be explored any further in this paper (see previous works^{34,49} for specific details on these jump conditions).

2.2 | Conservation of mass

The principle of conservation of mass for the continuum in an arbitrary spatial domain Ω (of boundary $\partial\Omega$ with spatial outward normal \mathbf{n}) can be expressed in a Eulerian integral form as follows:

$$\frac{d}{dt} \int_{\Omega} \rho \, d\Omega = 0, \quad (7)$$

where ρ is the mass density defined per unit of spatial volume, namely, $\rho = \rho(\mathbf{x}, t)$. Upon the use of the Reynolds transport theorem, the differential (or local) form of the above expression (7), in the case of smooth solutions, becomes

$$\frac{\partial \rho}{\partial t} + \nabla \cdot (\rho \mathbf{u}) = 0, \quad (8)$$

together with the jump conditions (in the case of nonsmooth solutions)^{34,50}

$$U[[\rho]] = [[\rho \mathbf{u}]] \cdot \mathbf{n} \quad (9)$$

across a discontinuity surface defined by a normal \mathbf{n} and speed U in the spatial or Eulerian space. As expected, substitution of the nonslip condition (6) into (9) yields $U = \mathbf{u} \cdot \mathbf{n}$, which defines the normal speed of the discontinuity front across a sudden change of density. Furthermore, substitution of the incompressibility constraint (5) into (8) results in $\frac{d\rho}{dt} = 0$, which confirms that the density must remain constant throughout the deformation.

2.3 | Conservation of linear momentum

The conservation of linear momentum for the continuum in an arbitrary spatial domain Ω (of boundary $\partial\Omega$ with spatial outward normal \mathbf{n}) can be expressed in an Eulerian integral form as follows:

$$\frac{d}{dt} \int_{\Omega} \rho \mathbf{u} \, d\Omega = \int_{\Omega} \rho \mathbf{g} \, d\Omega + \int_{\partial\Omega} \mathbf{t} \, da \quad (10)$$

where $\mathbf{t} = \boldsymbol{\sigma} \mathbf{n}$ is the traction vector, \mathbf{g} represents a force per unit of mass (ie, gravitational acceleration), and $\boldsymbol{\sigma}$ is the (symmetric) Cauchy stress tensor. It is customary (for incompressible and nearly incompressible materials) to establish an

additive decomposition of this tensor in terms of a deviatoric contribution $\boldsymbol{\sigma}'$ (eg, $\boldsymbol{\sigma}' : \mathbf{I} = 0$) and a volumetric contribution defined by $-p\mathbf{I}$ (with p being the scalar pressure field). Upon the use of the Reynolds transport theorem, the differential (or local) form of the above expression (10), in the case of smooth solutions, becomes

$$\frac{\partial(\rho\mathbf{u})}{\partial t} + \nabla \cdot (\rho\mathbf{u} \otimes \mathbf{u} + p\mathbf{I} - \boldsymbol{\sigma}') = \rho\mathbf{g}, \quad (11)$$

together with the jump conditions (for nonsmooth solutions) defined as

$$U[[\rho\mathbf{u}]] = [[\rho\mathbf{u} \otimes \mathbf{u} + p\mathbf{I} - \boldsymbol{\sigma}']]n \quad (12)$$

across a discontinuity surface defined by a normal \mathbf{n} and speed U in the spatial or Eulerian space. Proceeding in a similar manner to above Section 2.2, by means of the substitution of the nonslip condition (6) into (12) and making use of the fact that $U = \mathbf{u} \cdot \mathbf{n}$, it yields

$$[[p]] = \mathbf{n} \cdot [[\boldsymbol{\sigma}']]n, \quad (13)$$

which states that, in the absence of shock waves, the jump in pressure across a discontinuity must be balanced by the normal component of the deviatoric contribution to the traction vector.

2.4 | Conservation of deformation gradient

In the case of deformable solids, previous works^{34,35} provide additional conservation laws and jump conditions for the fundamental strain measures $\{\mathbf{F}, \mathbf{H}, J\}$ which, in conjunction with Equations (8) and (11), can render an enhanced system of conservation laws.* The introduction of additional geometric conservation laws have proven to be very efficient in circumventing the drawbacks of traditional low-order displacement-based formulations in the context of solid dynamics.^{33-35,51,52} This can be straightforwardly translated to the case of FSI applications.^{13,14,16}

For instance, the total Lagrangian conservation law for the deformation gradient \mathbf{F} can be written as $\frac{\partial \mathbf{F}}{\partial t} - \nabla_0 \cdot (\mathbf{u} \otimes \mathbf{I}) = 0$ (refer to previous works^{34,35} for further details). When this law is reexpressed by using a mixed Lagrangian-Eulerian formalism, it reduces to above Equation (4). All in all, in the case of incompressible materials (of interest in this paper), the three Equations (4), (5), and (11) constitute the final system of equations to be solved in terms of the unknown variables \mathbf{u} , p , $\boldsymbol{\sigma}'$, and \mathbf{F} (or \mathbf{I}).

2.5 | Constitutive equations

For closure of the above system of equations defined in the domain Ω , and in the case of incompressible materials, it is necessary to introduce appropriate constitutive models to relate $\boldsymbol{\sigma}'$ with \mathbf{F} (or \mathbf{I}), obeying the principles of objectivity⁴⁸ and thermodynamic consistency (via the Coleman-Noll procedure).⁵³

Two prototypical cases will be considered in this paper, although the approach pursued hereafter could be generalised to other constitutive models. First, for any time-varying Newtonian fluid occupying the domain $\Omega_f(t) \subset \Omega$, the deviatoric component of the Cauchy stress tensor $\boldsymbol{\sigma}'$ can be written as

$$\boldsymbol{\sigma}' = 2\mu\mathcal{I}' : \mathbf{d}; \quad \mathcal{I}' = \mathbf{I} - \frac{1}{3}(\mathbf{I} \otimes \mathbf{I}); \quad \mathbf{d} = \frac{1}{2}(\mathbf{l} + \mathbf{l}^T), \quad (14)$$

where μ denotes the shear viscosity of the fluid and \mathbf{d} the so-called strain rate tensor. Above Equation (14) can be further reduced for incompressible fluids (velocity divergence free) to $\boldsymbol{\sigma}' = 2\mu\mathbf{d}$. This constitutive model will be used for the numerical simulation presented in this paper to describe the behaviour of all fluid phases occupying the domain $\Omega_f(t) \subset \Omega$ (eg, air, water). Similarly, for deformable solid phases occupying the time-varying domain $\Omega_s(t) = \Omega \setminus \Omega_f(t)$, a hyperelastic incompressible solid will be considered. Specifically, for the numerical simulations presented in this paper the well-known incompressible neo-Hookean constitutive law will be employed, which is defined as

$$\boldsymbol{\sigma}' = GJ^{-5/3}\mathcal{I}' : \mathbf{b}; \quad \mathbf{b} = \mathbf{F}\mathbf{F}^T, \quad (15)$$

where G represents the shear modulus of the material and \mathbf{b} is the left Cauchy-Green deformation tensor.⁴⁸ In this case, it is interesting to remark that the evaluation of $\boldsymbol{\sigma}'$ requires the knowledge of the deformation gradient tensor \mathbf{F} , which can be related to the spatial velocity field via Equation (4). Following previous work developed by the authors, this will be the approach pursued in this paper.^{13,14,16} Traditionally, in immersed computational methodologies, the deformation gradient \mathbf{F} is obtained

*This can be useful to define a generalised convex entropy function necessary for the derivation of an alternative system of conservation laws in terms of entropy conjugates.^{34,35}

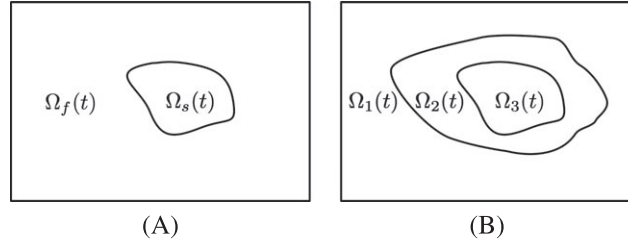


FIGURE 2 Possible distribution of phases within the spatial Eulerian domain Ω . A, $\Omega_s(t)$ denotes solid and $\Omega_f(t)$ fluid. B, $\Omega_a(t)$, $a = 1, 2, 3$, represent various phases; in this case, $\Omega_1(t) \cup \Omega_2(t) = \Omega_f(t)$ and $\Omega_3(t) \equiv \Omega_s(t)$

from Equation (1) directly, after time integration of the velocity field \mathbf{u} yields the spatial geometry \mathbf{x} .^{11,26} However, in the case of using a low-order discretisation scheme, this approach can lead to the appearance of locking behaviour, as reported in previous works,^{13,14} which is the reason why the additional Equation (4) is solved in a mixed-type manner.

2.6 | Eulerian governing equations

We are now in a position to combine all the equations presented above for the case of an (Eulerian description) comprised of “possibly” multiple time-varying n -subdomains (ie, air, water, and solid), namely, $\cup_{a=1}^n \Omega_a(t) = \Omega$, where the sets $\Omega_a(t)$, $a = 1, \dots, n$ are pairwise disjoint (eg, $\Omega_a(t) \cap \Omega_b(t) = \emptyset$ for two different phases $a \neq b$) (refer to Figure 2).

With respect to the governing equations, the only difference between the various phases stems from the constitutive model under consideration, which results in different expressions for the spatial divergence of the deviatoric stress tensor (11) (introduced herein as a new force field \mathbf{f}). Specifically, for a time-varying phase defined by a subdomain $\Omega_a(t) \subset \Omega$, the deviatoric force field \mathbf{f} can be obtained from Equations (14) and (15) as

$$\mathbf{f}(\mathbf{x}) = \begin{cases} \nabla \cdot (2\mu_a \mathbf{d}) & \text{in } \Omega_a(t) \cap \Omega_f(t) \\ \nabla \cdot (G_a J^{-5/3} \mathbf{I}' : \mathbf{b}) & \text{in } \Omega_a(t) \cap \Omega_s(t). \end{cases} \quad (16)$$

where μ_a or G_a represent the phase material properties. For the complete definition of the initial boundary value problem, initial and boundary (ie, essential $\partial\Omega_D$ and natural $\partial\Omega_N$) conditions must be specified ($\partial\Omega_D \cup \partial\Omega_N = \partial\Omega$ and $\partial\Omega_D \cap \partial\Omega_N = \emptyset$). Following is the set of balance equations that model the FSI problem:

$$\frac{\partial(\rho \mathbf{u})}{\partial t} + \nabla \cdot (\rho \mathbf{u} \otimes \mathbf{u}) = -\nabla p + \mathbf{f} + \rho \mathbf{g} \quad \text{in } \Omega \times [0, T] \quad (17a)$$

$$\nabla \cdot \mathbf{u} = 0 \quad \text{in } \Omega \times [0, T] \quad (17b)$$

$$\frac{d\mathbf{F}}{dt} = \mathbf{I}\mathbf{F} \quad \text{in } \Omega_s(t) \quad (17c)$$

$$\frac{d\mathbf{x}}{dt} = \mathbf{u} \quad \text{in } \Omega_s(t) \quad (17d)$$

$$\mathbf{u} = \bar{\mathbf{u}} \quad \text{on } \partial\Omega_D \times [0, T] \quad (17e)$$

$$-p\mathbf{I} + \boldsymbol{\sigma}' \mathbf{n} = \bar{\mathbf{t}} \quad \text{on } \partial\Omega_N \times [0, T] \quad (17f)$$

$$\mathbf{u} = \mathbf{u}_0 \quad \text{in } \bar{\Omega} \times \{0\} \quad (17g)$$

$$[[\mathbf{u}]] = \mathbf{0} \quad \text{on } \partial\Omega_a(t) \cap \partial\Omega_b(t) \quad (17h)$$

$$[[p]] = \mathbf{n} \cdot [[\boldsymbol{\sigma}']] \mathbf{n} \quad \text{on } \partial\Omega_a(t) \cap \partial\Omega_b(t), \quad (17i)$$

where \mathbf{u}_0 represents the initial velocity field and $\bar{\mathbf{u}}$ and $\bar{\mathbf{t}}$ are prescribed boundary velocity and traction vectors, respectively. The force field \mathbf{f} in (17a) is defined according to (16), where Equations (17c) and (17d) are only solved in the presence of a solid phase. The above set of Equations (16) and (17) define the initial boundary value problem expressed in a “nearly” complete Eulerian description, apart from Equations (17c) and (17d), which are expressed in a mixed Lagrangian-Eulerian description. The unknown fields of this set of equations are $\{\mathbf{u}, p\}$ in $\Omega \times [0, T]$ and $\{\mathbf{F}, \mathbf{x}\}$ in $\Omega_s(t)$. The explicit consideration of the jump conditions (17h) and (17i) requires the use of classical boundary-fitted FSI schemes to accurately track the evolution of the interface and fit the computational mesh accordingly.^{4,5}

3 | “ONE-FLUID” MODELLING

3.1 | “One-fluid” formulation

In the case of immersed computational methodologies, the explicit use of the jump conditions (17h) and (17i) is avoided by means of a “smooth regularisation” of the interface. For instance, for the n-phase incompressible fluid-solid continuum Ω (Eulerian description) defined above, the “smooth” density field ρ can be described as

$$\rho(\mathbf{x}, t) = \sum_{a=1}^n \rho_a H_a(\mathbf{x}, t), \quad (18)$$

where ρ_a is the density of the a-phase $\Omega_a(t)$ (assumed constant for simplicity) and $H_a(\mathbf{x}, t)$ is a smooth representation of the “sharp” indicator function for the a-phase.[†] It is thus possible to construct an n-dimensional vector field \mathbf{H}^\ddagger comprised of all smooth indicator functions H_a , namely, $[\mathbf{H}]_a = H_a$. The use of the vector field \mathbf{H} , allows the smooth “capturing” of the transition between the different phases comprising the continuum. A similar “smooth” representation to that of (18) can be written for the fluid viscosity field μ as

$$\mu(\mathbf{x}, t) = \sum_{a=1}^n \mu_a H_a(\mathbf{x}, t), \quad \mu_a = 0 \text{ in } \Omega_a(t) \cap \Omega_s(t) \quad (19)$$

where μ_a is the viscosity of the a-phase $\Omega_a(t)$ (assumed constant for simplicity). Notice that $\mu_a = 0$ in the case of a solid phase. The use of the “smooth” representations (18) and (19) in (17a) replaces the need to use the jump conditions (17h) and (17i), as they end up inherently included into the formulation (through the spatial gradient of the indicator function).⁵⁴ This approach is classically known as the “one-fluid” formulation in the context of multiphase flows⁵⁴ and is pursued in this paper. This formulation is named “one-fluid” because the underlying governing equations follow a similar pattern to those of the single-phase Navier-Stokes equations, yet it allows for the possibility of multiple phases including deformable solids. The formulation can be understood as a combination of the multiphase equations into a single “one-fluid” equation.

The “one-fluid” formulation relies on the correct identification of the interface between the different phases of the continuum so as to evaluate correctly the vector field \mathbf{H} . To identify the motion of an interface, two well-known techniques can be used, namely, the Lagrangian (tracking) particle method^{39,40} and the Eulerian (capturing) level set method.^{55,56} For instance, for a particle placed initially at location \mathbf{X}_s , its spatial position \mathbf{x}_s at time t can be obtained after time integration of the velocity field \mathbf{u} , noticing that

$$\frac{d\mathbf{x}_s(\mathbf{X}_s, t)}{dt} = \mathbf{u}(\mathbf{X}_s, t) = \mathbf{u}(\Phi^{-1}(\mathbf{x}_s, t), t). \quad (20)$$

This approach, suitable to monitor interfaces without topological changes, will be preferred in this paper for the tracking of immersed solid phases. Notice that for the evaluation of (20) a suitable interpolation technique is necessary to transfer the velocity field from the Eulerian description to the Lagrangian description, which will be presented in a subsequent section.

On the other hand, for fluid-fluid interfaces, this paper will employ the well-known level set method of Osher and Sethian,⁵⁵ later explored in the previous work⁵⁶ in the context of multiphase flows. In this Eulerian-based method, a scalar level set function $\phi_a = \phi_a(\mathbf{x}, t)$ is introduced for the a-phase $\Omega_a(t)$ as a signed distance function to the time-varying interface Γ_a^t between this and the rest of phases comprising the continuum, namely,

$$\phi_a(\mathbf{x}, t) = \text{sgn} (d(\mathbf{x}, \Gamma_a^t)), \quad (21)$$

where $d(\mathbf{x}, \Gamma_a^t)$ denotes the distance from \mathbf{x} to Γ_a^t . The interface Γ_a^t coincides with the zero-contour of the level set function (ie, $\Gamma_a^t \equiv \mathbf{x}$ such that $\phi_a(\mathbf{x}, t) = 0$). For an incompressible continuum,[§] the advection of the level set is achieved by solution of the evolution or transport equation:

$$\frac{\partial \phi_a}{\partial t} + \nabla \cdot (\mathbf{u} \phi_a) = 0. \quad (22)$$

The evaluation of a-phase smooth indicator function H_a follows naturally as $H_a(\mathbf{x}, t) = H(\phi_a(\mathbf{x}, t))$, where H is a smooth presentation of the Heaviside step function. In the same manner as the vector field \mathbf{H} was previously introduced, it is also possible to define $\boldsymbol{\phi}$ as the vector field containing the set of n level set functions ϕ_a as $[\boldsymbol{\phi}]_a = \phi_a$. It is now possible to present

[†]The sharp indicator function $H_a(\mathbf{x}, t)$ would be defined as $H_a(\mathbf{x}, t) = \begin{cases} 1 & \text{if } \mathbf{x} \in \Omega_a \\ 0 & \text{elsewhere} \end{cases}$.

[‡]Not to be confused with the co-factor of the deformation, the latter not to be used henceforth.

[§]The original level set equation reads $\frac{\partial \phi_a}{\partial t} + \mathbf{u} \cdot \nabla \phi_a = 0$.

the complete set of equations governing the “one-fluid” formulation for an arbitrary control volume Ω as

$$\int_{\Omega} \frac{\partial(\rho \mathbf{u})}{\partial t} d\Omega + \int_{\partial\Omega} (\rho \mathbf{u} \otimes \mathbf{u} + p \mathbf{I}) \mathbf{n} da - \int_{\Omega} (\mathbf{f} + \rho \mathbf{g}) d\Omega = \mathbf{0} \quad \text{in } \Omega \times [0, T] \quad (23a)$$

$$\nabla \cdot \boldsymbol{\sigma}' = \nabla \cdot \mu \left(\frac{1}{2} (\nabla \mathbf{u} + (\nabla \mathbf{u})^T) \right) =: \mathbf{f} \quad \text{in } \Omega \times [0, T] \quad (23b)$$

$$\int_{\partial\Omega} \mathbf{u} \cdot \mathbf{n} da = 0 \quad \text{in } \Omega \times [0, T] \quad (23c)$$

$$\frac{d\mathbf{F}}{dt} = \mathbf{I}\mathbf{F} \quad \text{in } \Omega_s(t) \quad (23d)$$

$$\frac{d\mathbf{x}}{dt} = \mathbf{u} \quad \text{in } \Omega_s(t) \quad (23e)$$

$$\nabla \cdot \boldsymbol{\sigma}' = \nabla \cdot (G_s(\det \mathbf{F})^{-5/3} \mathbf{I}' : (\mathbf{F}\mathbf{F}^T)) =: \mathbf{f} \quad \text{in } \Omega_s(t) \quad (23f)$$

$$\forall a = 1 \dots n \quad \int_{\Omega} \frac{\partial \phi_a}{\partial t} d\Omega + \int_{\partial\Omega} \phi_a (\mathbf{u} \cdot \mathbf{n}) da = 0 \quad \text{in } \Omega \times [0, T] \quad (23g)$$

$$\mathbf{u} = \bar{\mathbf{u}} \quad \text{on } \partial\Omega_D \times [0, T] \quad (23h)$$

$$-p\mathbf{I} + \boldsymbol{\sigma}'\mathbf{n} = \bar{\mathbf{t}} \quad \text{on } \partial\Omega_N \times [0, T] \quad (23i)$$

$$\mathbf{u} = \mathbf{u}_0 \quad \text{in } \bar{\Omega} \times \{0\} \quad (23j)$$

$$\phi_a = [\phi_0]_a \quad \text{in } \bar{\Omega} \times \{0\}, \quad (23k)$$

where the smooth fields ρ (23a) and μ (to be used for the computation of \mathbf{f} in (23b)) are defined in (18) and (19) and the essential (23h) and natural (23i) boundary conditions are incorporated into (23a) wherever necessary. Finally, Equation (23k) represents the initial conditions for the level set vector field $\boldsymbol{\phi}$. The unknown fields of this set of equations are $\{\mathbf{u}, p, \boldsymbol{\phi}\}$ in $\Omega \times [0, T]$ and $\{\mathbf{F}, \mathbf{x}\}$ in $\Omega_s(t)$. The use of the integral form representation in (23a), (23c), and (23g) is convenient as, firstly, will become the starting point of the spatial discretisation technique presented in the following section, and secondly, it is usually preferred in case of using sharp indicator functions for every phase as it avoids their definition in the sense of a distribution.

In traditional immersed computational methodologies (including the pioneering IBM),^{6-14,16} the immersed body force \mathbf{f}_{IBM} is evaluated as

$$\mathbf{f}_{\text{IBM}} = \underbrace{\nabla \cdot (\boldsymbol{\sigma}'_s - \boldsymbol{\sigma}'_f)}_{\mathbf{f}_{\mu}} + \underbrace{(\rho_s - \rho_f)\mathbf{g} - (\rho_s - \rho_f) \frac{d\mathbf{u}}{dt}}_{\mathbf{f}_{\rho}} \quad \text{in } \Omega_s(t), \quad (24)$$

which is composed of the following two contributions. Firstly, \mathbf{f}_{μ} denotes the difference between the deviatoric stresses of the deformable solid and those of the underlying fluid. The fluid stress contribution $-\boldsymbol{\sigma}'_f$ is necessary to counterbalance the “fictitious” viscous effects introduced by the underlying fluid in the overlapping area between solid and fluid. Secondly, \mathbf{f}_{ρ} gathers the inertial and body force differences of the solid with the underlying fluid because of nonmatching densities. Notice that both force contributions \mathbf{f}_{μ} and \mathbf{f}_{ρ} are computed in a fully Lagrangian manner in $\Omega_s(t)$, requiring appropriate interpolation-spreading operators.

In the case of the “one-fluid” formulation pursued in this paper, it is noteworthy to observe that “only” the deviatoric stress force component stemming from the presence of solid deformable phases in $\Omega_s(t)$, namely, $\nabla \cdot \boldsymbol{\sigma}'_s$, is computed via a mixed Lagrangian-Eulerian approach (refer to Equations (23d)-(23f)); elsewhere, a fully Eulerian approach is used. For instance, the use of an indicator function approach to reconstruct a smooth representation of the density field enables the modelling of both inertial and gravity effects in a fully Eulerian manner.

For most FSI problems, large values of \mathbf{f}_{μ} and \mathbf{f}_{ρ} can limit the “efficient” use of explicit time-stepping schemes, which is the case of immersed solids with a large shear modulus or immersed phases with large density ratios (eg, hydrodynamic applications), respectively. In this paper, we have adopted the approach followed by Gil et al,^{13,16,57,58} where a fixed-point iteration strategy was used for the tracking of the deformable solid (23d) and (23e) and the evaluation of its deviatoric force term (23f), whilst the rest of the terms are treated in a fully implicit Eulerian manner. This strategy has been shown to be appropriate for the numerical examples presented in this paper. However, for stiffer problems, a fully implicit approach could also be adopted.⁵⁹ Alternatively, for the FSI problem with small density ratios, a fully explicit approach can be used.⁶⁰

4 | NUMERICAL TECHNIQUE

4.1 | Multiphase Eulerian background solver

The space-time discretisation technique used in this paper is that of Gil et al,^{13,16} but expanded hereafter to incorporate the transport of the level set function $\phi_a(x, t)$ for each a-phase and the definition of the smooth Heaviside function $H(\phi_a)$. The formulation is briefly described for completeness.

A two-dimensional Cartesian discretisation of the incompressible Eulerian continuum is adopted in conjunction with a staggered low (second) order finite volume approach. Let Ω^{A_x} and Ω^{A_y} be two families of control volumes associated with the Cartesian components of the velocity u^{A_x} and v^{A_y} , with an arrangement similar to that of a marker-and-cell (MAC) grid. Harlow and Welch⁶¹ proposed the use of a special grid for incompressible flow computations. This especially defined grid decomposes the computational domain into cells with velocities defined on the cell faces and scalar pressure defined at cell centres (see Figure 3). Here, A_x and A_y denote the fluid cell edges perpendicular to the ox and oy Cartesian axes, respectively, and u^{A_x} and v^{A_y} their corresponding normal edge velocities (refer to Figure 3A,B).

Consideration of arbitrary internal control volumes Ω^{A_x} and Ω^{A_y} and following a standard staggered control volume approach permits to split the conservation of linear momentum Equation (23a) into

$$\frac{d(\rho u^{A_x})}{dt} \Omega^{A_x} + \int_{\partial \Omega^{A_x}} \mathbf{F}_u \cdot \mathbf{n} da - (f_x^{A_x} + \rho g_x^{A_x}) \Omega^{A_x} = 0, \quad (25a)$$

$$\frac{d(\rho v^{A_y})}{dt} \Omega^{A_y} + \int_{\partial \Omega^{A_y}} \mathbf{F}_v \cdot \mathbf{n} da - (f_y^{A_y} + \rho g_y^{A_y}) \Omega^{A_y} = 0, \quad (25b)$$

where $\{g_x^{A_x}, g_y^{A_y}\}$ represents the edge Cartesian components of the body force \mathbf{g} , $\{f_x^{A_x}, f_y^{A_y}\}$ represents the edge Cartesian components of the body force \mathbf{f} , and Ω^{A_x} and Ω^{A_y} denote the size of the corresponding control volumes. In addition, $\{\mathbf{F}_u, \mathbf{F}_v\}$ represent numerical interface fluxes defined as

$$\mathbf{F}_u = \rho \mathbf{u} \mathbf{u} + p \mathbf{e}_x, \quad \mathbf{F}_v = \rho \mathbf{v} \mathbf{v} + p \mathbf{e}_y, \quad \mathbf{u} = [u, v]^T, \quad (26)$$

with $\{\mathbf{e}_x, \mathbf{e}_y\}$ the standard Cartesian basis and where the convective components of the numerical fluxes (26) are obtained using an appropriate stabilised convective approximation (ie, SMART,⁶² HPLA,⁶³ or QUICK⁶⁴), which minimises numerical diffusion, avoids the creations of spurious oscillations, and reduces the total variation of the solution by accounting for the transportive nature of the fluid.

In addition to the two families of control volumes defined above, another family, namely, Ω^A , is associated with the level set fields ϕ_a^A describing the interface of each a-phase. These variables are stored, in conjunction with the pressure field p^A , at the cell centroids (see Figure 3C). The discretisation of the level set Equation (22) for the a-phase yields

$$\forall a = 1 \dots n \quad \frac{d\phi_a^A}{dt} \Omega^A + \int_{\partial \Omega^A} \phi_a (\mathbf{u} \cdot \mathbf{n}) da = 0, \quad (27)$$

where $|\Omega^A|$ denotes the size of the control volume and the numerical flux is also (consistently) discretised using any of the stabilised schemes listed above (ie, SMART, HPLA, QUICK). The accurate transport of the level set vector field $\boldsymbol{\phi}$ is necessary to correctly evaluate the indicator function vector field \mathbf{H} in above Equations (25a) and (25b) when evaluating the smooth density (18) and viscosity (19) fields. Wherever necessary, re-initialisations strategies for the level set fields can be employed

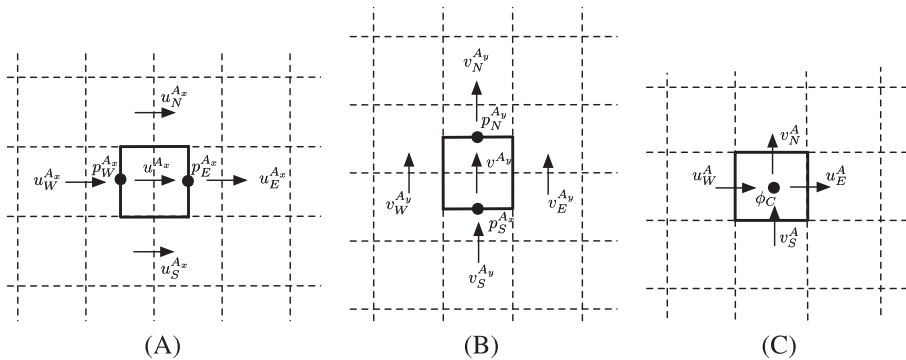
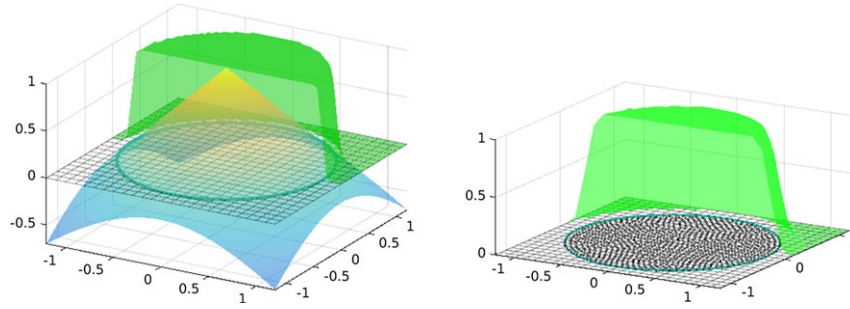


FIGURE 3 The notation used for a standard staggered MAC mesh. A, Control volume Ω^{A_x} for velocity u . B, Control volume Ω^{A_y} for velocity v ; C, Control volume Ω^A for level set ϕ



(A) Constructed from level set $\phi = x^2 + y^2 - 1$ (B) Constructed via integration points and smooth kernel functions

FIGURE 4 Illustration of construction of the indicator function for a circle, centred at $[0, 0]$ with radius $r = 1$ and representation of the cross section of the indicator function [Colour figure can be viewed at wileyonlinelibrary.com]

as in the work of Sussman et al.⁵⁶ to guarantee the distance function property of the level set fields. Knowledge of the discrete level set field ϕ_a^A permits the evaluation of the discrete indicator function field H_a^A and thus evaluation of the discrete density field ρ^A (18) as $\rho^A = \sum_{a=1}^n \rho_a H_a^A$ and the discrete viscosity field μ^A (19) as $\mu^A = \sum_{a=1}^n \mu_a H_a^A$.

Finally, and as presented in the work of Gil et al.,¹⁶ the divergence free integral constraint (23c) is enforced in every control volume Ω^A following a fractional step approach⁶⁵

$$\int_{\partial\Omega^A} \mathbf{u} \cdot \mathbf{n} \, da = 0, \quad (28)$$

so that the discrete pressure field p^A can thus be obtained.

4.2 | Indicator function

As stated above, the evaluation of the smooth fields ρ and μ requires the computation of the indicator vector field \mathbf{H} . This can be done in two different manners, depending on the way in which the interface is followed (refer to Equations (20) and (22)). Firstly, following the work of Sussman et al.,⁵⁶ the components of \mathbf{H} (eg, $[\mathbf{H}]_a = H_a$) can be defined in terms of a smooth representation of the Heaviside function H as

$$H_a(\mathbf{x}, t) = H(\phi_a(\mathbf{x}, t)) = \begin{cases} \frac{1}{2} \left(1 + \frac{\phi_a}{\epsilon} + \frac{1}{\pi} \sin(\pi \frac{\phi_a}{\epsilon}) \right) & \text{if } |\frac{\phi_a}{\epsilon}| \leq 1 \\ 0 & \text{if } \frac{\phi_a}{\epsilon} < -1 \\ 1 & \text{if } \frac{\phi_a}{\epsilon} > 1 \end{cases} \quad (29)$$

where ϵ is the parameter representing the smearing bandwidth and ϕ_a denotes the corresponding a-phase level set value. The approximation of the indicator function sharply changes from zero to one over the smearing interface, describing a smooth transition zone from one phase to the next. Evaluation of the indicator function for the control volume Ω^A can be straightforwardly obtained as $H_a^A = H(\phi_a^A)$ combining Equations (27) and (29).

Alternatively, a smooth indicator function H_s defined for an “immersed” phase Ω_s contained within Ω can also be constructed from the “spreading” operation S to the underlying Eulerian grid of a unit constant field $f = 1$ defined on Ω_s . Provided the phase Ω_s is tracked via integration points (or material particles) \mathbf{x}^{a_p} , the indicator function H_s can then be evaluated at the Eulerian control volume Ω^A as

$$H_s^A = S(f = 1)|_{\Omega_s^A} \simeq \frac{1}{|\Omega^A|} \sum_{a_p} W^{a_p} \hat{\delta}^A(\mathbf{x}^{a_p}), \quad (30)$$

where $\hat{\delta}^A(\mathbf{x}^{a_p})$ is a smooth interpolation kernel functions $\hat{\delta}^A$ centred in the centroid of the control volume Ω^A and evaluated at the integration point a_p . For the examples presented in this paper, the smooth kernel functions used are those defined in the work of Gil et al.^{13,16} Figure 4 illustrates the construction of the indicator function for the specific case of a circle using both a level set approach (29) and a material particle approach (30). The circle is centred at $[0, 0]$ and has a radius of 1. The cross section of the constructed indicator function is depicted in Figure 4 (in green).

4.3 | Solid Cauchy stresses via immersed structural potential method

The solid phases defined by Ω_s are modelled in a Lagrangian manner as a collection of integration points a_p , moving from an initial position \mathbf{X}^{a_p} to the spatial position \mathbf{x}^{a_p} at time t (20). The velocity of every solid integration point is obtained after suitable definition of an interpolation operator from the background Eulerian fluid (edges) to the Lagrangian solid (integration points). Specifically, the velocity \mathbf{u} at any integration point a_p is evaluated as

$$\mathbf{u}^{a_p} = [\mathbf{u}^{a_p}, \mathbf{v}^{a_p}]^T; \quad \mathbf{u}^{a_p} = \sum_{A_x} u^{A_x} \hat{\delta}^{A_x}(\mathbf{x}^{a_p}); \quad \mathbf{v}^{a_p} = \sum_{A_y} v^{A_y} \hat{\delta}^{A_y}(\mathbf{x}^{a_p}), \quad (31)$$

where $\hat{\delta}^{A_x}(\mathbf{x}^{a_p})$ and $\hat{\delta}^{A_y}(\mathbf{x}^{a_p})$ are smooth interpolation kernel functions as defined by Gil et al.^{13,16} Time integration of above equation yields the current geometry \mathbf{x}^{a_p} .

As stated above, in conventional immersed methodologies,^{12,66} the fibre map \mathbf{F} is obtained upon material differentiation of the spatial configuration, namely, $\mathbf{F} := \nabla_0 \mathbf{x}$. Unfortunately, this leads to lower spatial resolution of structural stresses, the noncompliance with the kinematic constraint $J = 1$, and the possible appearance of locking behaviour (see Hesch et al,¹⁴ Section 5.3, page 62, for numerical evidence). To overcome these shortcomings, the deformation gradient \mathbf{F} is obtained after time integration of Equation (17c) is performed. With that in mind, the velocity gradient tensor \mathbf{l} can be defined in a_p as

$$\mathbf{l}^{a_p} = \left[\sum_{A_x} u^{A_x} \nabla \hat{\delta}^{A_x}(\mathbf{x}^{a_p}), \sum_{A_y} v^{A_y} \nabla \hat{\delta}^{A_y}(\mathbf{x}^{a_p}) \right]^T, \quad (32)$$

by taking advantage of the interpolating kernel functions. Finally, a tailor-made structure preserving time integration scheme for Equation (17c) is presented by Gil et al^{13,16} to obtain the deformation gradient at a_p , namely, \mathbf{F}^{a_p} . After evaluation of the deviatoric stress at the integration point $\sigma^{I a_p}$ via (15), a variationally consistent procedure to obtain the body forces $\{f_x^{A_x}, f_y^{A_y}\}$ in (25a) and (25b) is derived by Gil et al^{13,16} and written below as

$$f_x^{A_x} = \frac{1}{\Omega^{A_x}} \sum_{a_p} W^{a_p} \sigma^{I a_p} \nabla \hat{\delta}^{A_x}(\mathbf{x}^{a_p}); \quad f_y^{A_y} = \frac{1}{\Omega^{A_y}} \sum_{a_p} W^{a_p} \sigma^{I a_p} \nabla \hat{\delta}^{A_y}(\mathbf{x}^{a_p}), \quad (33)$$

where the details regarding the determination of the weight W^{a_p} can be found in the work of Gil et al.^{13,16} This approach enables the direct computation of immersed solid body forces at the Eulerian grid from the solid integration points, without having to resort to the use of an intermediate mesh describing the solid phase. In contrast, conventional immersed methodologies employ a two-step approach to evaluate the immersed body forces, which relies on the existence of a classical finite element discretisation of the immersed solid phase in terms of nodes and elements, as presented by Zhang et al¹² or Bardenhagen et al.⁶⁷

4.4 | Surface tension

Accurate computation of surface tension effects is one of the most important aspects in the numerical simulation of small scale multiphase problems.⁵⁴ Surface tension effects require the modification of the jump conditions (12) and (13) accordingly. In methods based on the ‘‘one-phase’’ formulation, the surface tension is usually added as a body force concentrated in a band around the interface at the discrete level,⁵⁴ defined for the interface of the a-phase as

$$\mathbf{f} = \gamma \kappa(\phi_a) \mathbf{n}(\phi_a) \hat{\delta}(\phi_a) \quad (34)$$

where κ is the surface curvature, \mathbf{n} is the outward unit normal across the interface, $\hat{\delta}$ is a smooth representation of the Dirac delta distribution, and γ is the so-called surface tension coefficient (physical property). Above magnitudes $\{\kappa, \mathbf{n}, \hat{\delta}\}$ are typically evaluated taking advantage of the level set function, namely,

$$\mathbf{n} = \frac{\nabla \phi_a}{\|\nabla \phi_a\|}; \quad \kappa = -\nabla \cdot \left(\frac{\nabla \phi_a}{\|\nabla \phi_a\|} \right), \quad (35)$$

and in the numerical examples presented in the paper, $\hat{\delta}(\phi_a)$ is defined consistently with (29)⁵⁶ as

$$\hat{\delta}(\phi) = \begin{cases} \frac{1}{2\epsilon} (1 + \cos(\pi \frac{\phi}{\epsilon})) & \text{if } |\frac{\phi}{\epsilon}| \leq 1 \\ 0 & \text{if } |\frac{\phi}{\epsilon}| > 1 \end{cases}, \quad (36)$$

where above Equations (34) and (35) can be straightforwardly adapted to the specific spatial discretisation presented above.

4.5 | Algorithm

For completeness, the set of discrete equations of the overall “one-fluid” methodology used in this paper is presented below. Upon the use of a simple fixed-point iterative scheme, the coupled FSI equations can be solved to advance from time step n to $n + 1$ in an iterative fashion to ensure the complete coupling of the fluid and solid equations. By computing a residual norm based on the difference between the divergence of the deviatoric Cauchy stress tensor in two successive iterations k and $k + 1$, namely, $\|f_{k+1}^{n+1} - f_k^{n+1}\| / \|f^n\|$, a convergence criterion can be easily established to progress to the following iteration $k + 2$ (if not yet converged) or time step $n + 2$ (if convergence is accomplished). As in the works of Gil et al,^{13,16} the Navier-Stokes equations are solved via a fractional step approach, where the unknown pressure field is obtained through an efficient preconditioned conjugate gradient anisotropic Poisson solver from the Hypre Library.⁶⁸

Once the velocity field $\mathbf{u}|_{k+1}^{n+1}$ is known, the level set equations can be straightforwardly updated although a Crank-Nicholson step leading to the evaluation of the smooth density and viscosity fields as

$$\rho^A|_{k+1}^{n+1} = \sum_{a=1}^n \rho_a H(\phi_a^A|_{k+1}^{n+1}); \quad \mu^A|_{k+1}^{n+1} = \sum_{a=1}^n \mu_a H(\phi_a^A|_{k+1}^{n+1}), \quad (37)$$

which permit the evaluation of the force field $\{f_x^{A_x}|_{k+1}^{n+1}, f_y^{A_y}|_{k+1}^{n+1}\}$ in the case of fluid phases, after applying the discrete divergence operator to the deviatoric stress tensor obtained via Equation (14). Consideration of surface tension effects can also be incorporated at this stage.

Alternatively, in the case of solid phases, integration points are tracked in a Lagrangian manner after suitable interpolation \mathcal{I} of the Eulerian velocity field (and its spatial gradient) as

$$\mathbf{u}^{a_p}|_{k+1}^{n+1} = \mathcal{I}(\mathbf{u}|_{k+1}^{n+1})(\mathbf{x}^{a_p}|_k^{n+1}); \quad \mathbf{l}^{a_p}|_{k+1}^{n+1} = \nabla \mathcal{I}(\mathbf{u}|_{k+1}^{n+1})(\mathbf{x}^{a_p}|_k^{n+1}). \quad (38)$$

The geometrical position of these integration points can be obtained via trapezoidal integration and the deformation gradient tensor is evaluated through a structured preserving algorithm described in the works of Gil et al^{13,16} and formulated below as

$$\mathbf{F}^{a_p}|_{k+1}^{n+1} = e^{(\Delta t \mathbf{l}^{a_p}|_{k+1}^{n+1})} \mathbf{F}^{a_p}|_k^n. \quad (39)$$

Finally, deviatoric stresses (15) and immersed body forces can be computed as

$$\boldsymbol{\sigma}^{a_p}|_{k+1}^{n+1} = \mathcal{G}(\mathbf{F}^{a_p}|_{k+1}^{n+1}) \quad (40)$$

and

$$f_x^{A_x}|_{k+1}^{n+1} = \frac{1}{|\Omega^{A_x}|} \sum_{a_p} W^{a_p} \boldsymbol{\sigma}^{a_p}|_{k+1}^{n+1} \nabla \hat{\delta}^{A_x}(\mathbf{x}^{a_p}|_{k+1}^{n+1}); \quad (41a)$$

$$f_y^{A_y}|_{k+1}^{n+1} = \frac{1}{|\Omega^{A_y}|} \sum_{a_p} W^{a_p} \boldsymbol{\sigma}^{a_p}|_{k+1}^{n+1} \nabla \hat{\delta}^{A_y}(\mathbf{x}^{a_p}|_{k+1}^{n+1}). \quad (41b)$$

At this stage, the new immersed body forces $\{f_x^{A_x}|_{k+1}^{n+1}, f_y^{A_y}|_{k+1}^{n+1}\}$ are compared against those in the previous iteration to establish convergence within the time step.

5 | NUMERICAL EXAMPLES

In the following section, a series of two-dimensional numerical examples will be examined to assess the applicability and robustness of the proposed “one-fluid” algorithm, benchmarking it against available published numerical and experimental results.

5.1 | Two-phase flow benchmark

The aim of this section is to validate the two-phase flow solver in the absence of an immersed deformable structure.

5.1.1 | Classical dam break problem

The dam break problem is a well documented example,⁶⁹⁻⁷⁴ which simulates the sudden collapse of a (square shaped) column of water onto a horizontal surface as a result of the effect of gravity. The general description of the problem is presented in Figure 5. The main objective of this problem is the simulation of the transient flow of two fluids (ie, air and water) separated by a sharp interface, where surface tension effects are disregarded. Insofar as the two-phase fluid solver is formulated following an immersed-based approach, the physical properties of the two fluids are smoothed across the sharp interface. This problem

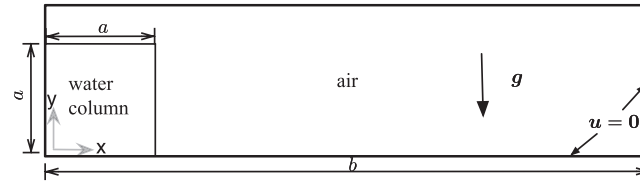


FIGURE 5 Schematics of the initial conditions for the dam break problem ($a = 1\text{ m}$; $b = 5\text{ m}$)

TABLE 1 Physical properties of water and air for the classical dam break problem

Water Density	Air Density	Water Viscosity	Air Viscosity
$\rho_w = 1000\text{ kg/m}^3$	$\rho_a = 1\text{ kg/m}^3$	$\mu_w = 10^{-3}\text{ Pa s}$	$\mu_a = 10^{-5}\text{ Pa s}$

has been thoroughly studied at experimental^{69,70} and numerical⁷¹⁻⁷⁴ levels, and it is widely used by the scientific community for the benchmarking of new algorithms.

For the numerical results presented herein, the side of the (square) water domain is initially prescribed as $a = 1\text{ m}$ (see Figure 5). The water phase is fully embedded inside a rectangular domain of base length $b = 5\text{ m}$. The height of the underlying rectangular domain must be chosen large enough so as to not having an effect in the simulation. With that in mind, for the results presented in this paper, this height was chosen as $h = 1.25\text{ m}$. Nonslip boundary conditions are considered for all the sides of the rectangular domain. The fluid properties of both phases (water and air will be referred by the subscripts w and a , respectively) are listed in Table 1 below.

Figure 6 illustrates a sequence of snapshots of the free surface position as a function of time. The predicted heights and the surge front location of the collapsed water are plotted against the dimensionless time $\tau = t \sqrt{h/g}$, as reported by Martin and Moyce.⁶⁹ In Figure 7, very good agreement can be observed between the numerical simulation obtained using the proposed algorithm and the experimental⁷⁰ and published numerical results⁷⁴ available in the literature. As can be observed, with mesh refinement, the presented results converge extremely well to the latest experimental data.

5.1.2 | Bubble rising in a partially filled container

The second benchmark problem is described by a fluid bubble placed inside a container partially filled with fluid of higher density. The initially circular bubble of diameter $D = 0.04\text{ m}$ is placed inside a computational domain defined by a rectangle $\Omega = [0, 3D] \times [0, 3.5D]$. Initially, a fluid layer of size D corresponding to the fluid of lower density rests above the $2.5D$ deep higher density fluid. The bubble is immersed with its centre located at a distance D below the free surface. The geometrical description of the problem can be found in Figure 8. Nonslip boundary conditions are considered for all the sides of the rectangular domain.

The bubble is considered to be made up of a fluid phase termed “fluid 2” of density ρ_2 , which progressively rises inside the container, which is partially filled with a fluid phase termed “fluid 1” of density ρ_1 (with density ratio $\rho_1 = 2\rho_2$). The upper section of the container, of height $D = 0.04\text{ m}$, is considered to be filled with the “fluid 2” phase. The Reynolds number (Re) and the Weber number (We) are defined by Zhao et al⁷¹ as

$$Re = \frac{\rho_1 \sqrt{g} D^{1.5}}{\mu_1}, \quad We = \frac{\rho_1 g D^2}{\gamma}, \quad (42)$$

where $\rho_1(\rho_2)$ is the density of “fluid 1”(“fluid 2”), g is the gravitational acceleration, D is the diameter of the bubble, $\mu_1(\mu_2)$ is the dynamic viscosity of “fluid 1”(“fluid 2”), and γ is the surface tension coefficient. In the following, two test cases are considered, namely, test case 1 does not consider the surface tension effect whilst test case 2 does (Table 2).

The time sequence of the rising bubble is shown in Figure 9, for the test case without surface tension, and in Figure 10, for the test case with surface tension. In both figures, numerical results are compared against those reported by Zhao et al.⁷¹ In both simulations, a mesh of 120×140 cells was used with $\Delta t = 5 \times 10^{-4}\text{ s}$. As it can be observed, an excellent agreement with the results of Zhao et al⁷¹ is shown in both cases, where very noticeable differences are observed in the dynamics of the interface.

5.1.3 | Bubble rising in a fully filled container

In this dimensionless problem, we consider the case of a fluid bubble (“fluid 2”) rising inside a container fully filled with a fluid of higher density (“fluid 1”). This quantitative validation for a two-phase problem was proposed by Hysing et al.⁷⁵ The initial

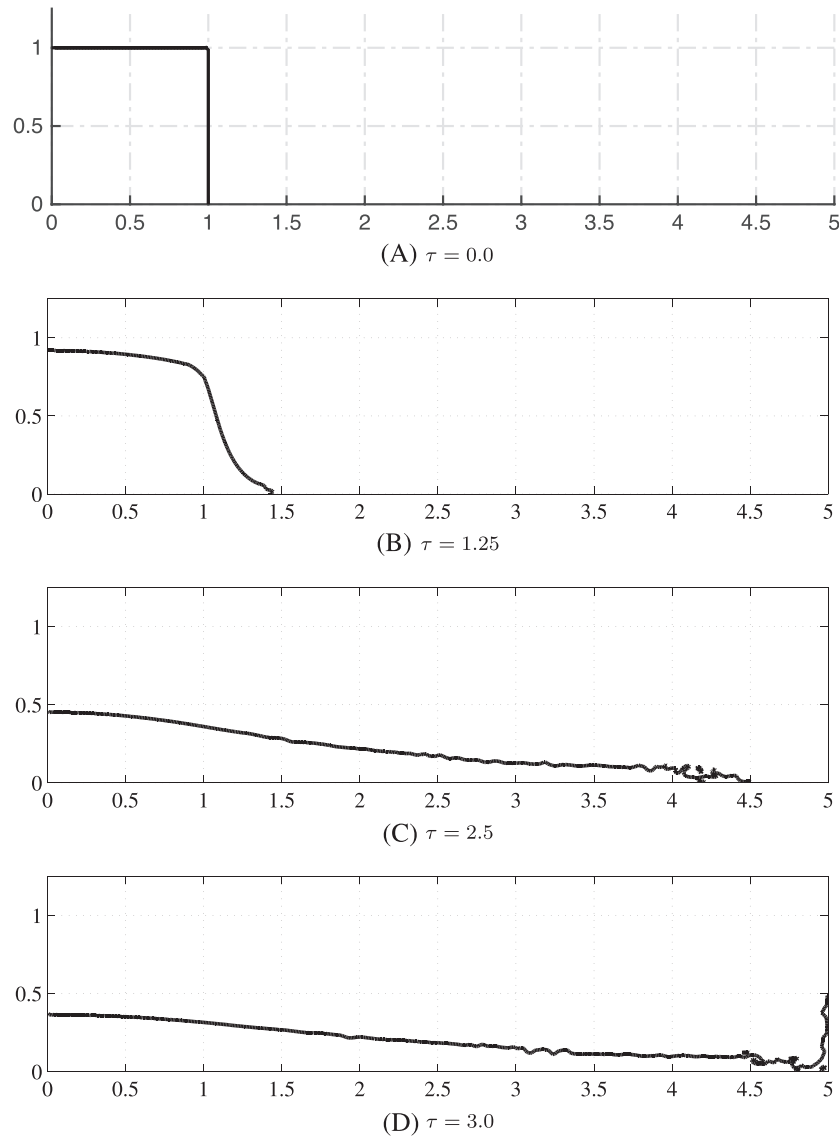


FIGURE 6 Predicted free surface evolution at different dimensionless time steps τ obtained for a mesh of 512×128 cells with dimensionless $\Delta\tau = 2 \times 10^{-4}$. A, $\tau = 0.0$. B, $\tau = 1.25$. C, $\tau = 2.5$. D, $\tau = 3.0$. The material parameters are as follows: water density $\rho_w = 1000 \text{ kg/m}^3$, air density $\rho_a = 1 \text{ kg/m}^3$, water viscosity $\mu_w = 10^{-3} \text{ Pa s}$, and air viscosity $\mu_a = 10^{-5} \text{ Pa s}$ (refer to Figure 5 and Table 1)

configuration consists of a circular bubble of radius $r = 0.25$ centred at $[0.5, 0.5]$ in a rectangular domain $\Omega = [0, 1] \times [0, 2]$. The geometrical description of the problem is presented in Figure 11.

The density of the fluid bubble is smaller than that of the surrounding fluid ($\rho_2 < \rho_1$). The nonslip boundary condition ($\mathbf{u} = \mathbf{0}$) is used at the top and bottom boundaries, whereas the free slip condition $\mathbf{u} \cdot \mathbf{n} = 0$ is imposed on the vertical walls (being \mathbf{n} the outward unit normal). Computations were conducted until time $t = 3$. The Reynolds number and the Eotvos number are defined by Hysing et al.⁷⁵ as

$$Re = \frac{\rho_1 \sqrt{g}(2r)^{2/3}}{\mu_1}, \quad E_0 = \frac{4\rho_1 g r^2}{\gamma}, \quad (43)$$

where $\rho_1(\rho_2)$ is the density of “fluid 1”(“fluid 2”), g is the gravitational acceleration, r is the radius of the bubble, $\mu_1(\mu_2)$ is the dynamic viscosity of “fluid 1”(“fluid 2”), and γ is the surface tension coefficient. Two test cases are analysed, and Table 3 summarises the physical properties considered in both of them.

To benchmark the numerical solution, a series of physical magnitudes of interest are introduced by Hysing et al.,⁷⁵ including the centre of mass of the bubble, its mean rising velocity, and the so-called circularity of the bubble (to be defined below).

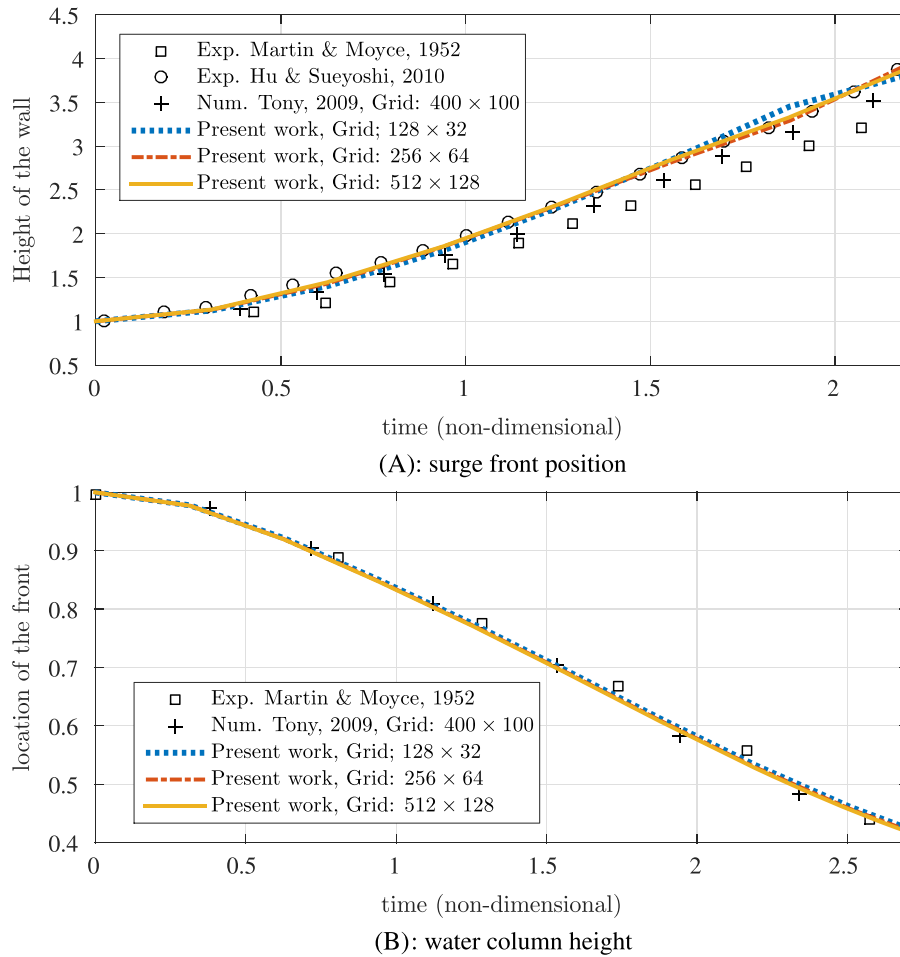


FIGURE 7 Comparison of the surge front location and the water column height with experimental data and numerical results. The corresponding dimensionless time refinement is as follows: $\Delta\tau = 8 \times 10^{-4}$, $\Delta\tau = 4 \times 10^{-4}$, and $\Delta\tau = 2 \times 10^{-4}$. The material parameters are as follows: water density $\rho_w = 1000 \text{ kg/m}^3$, air density $\rho_a = 1 \text{ kg/m}^3$, water viscosity $\mu_w = 10^{-3} \text{ Pa s}$, and air viscosity $\mu_a = 10^{-5} \text{ Pa s}$ (refer to Figure 5 and Table 1) [Colour figure can be viewed at wileyonlinelibrary.com]

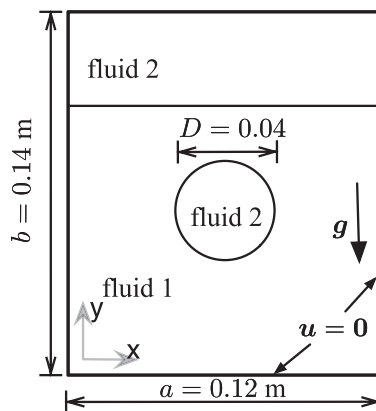


FIGURE 8 Schematic diagram of the two-dimensional container partially filled with fluid phases 1 and 2

- Centre of mass. The position of the centre of mass is used to track the translation of the bubble as a function of time and is defined as

$$\mathbf{x}_c = \frac{\int_{\Omega_2} \mathbf{x} \, dv}{\int_{\Omega_2} dv}. \tag{44}$$

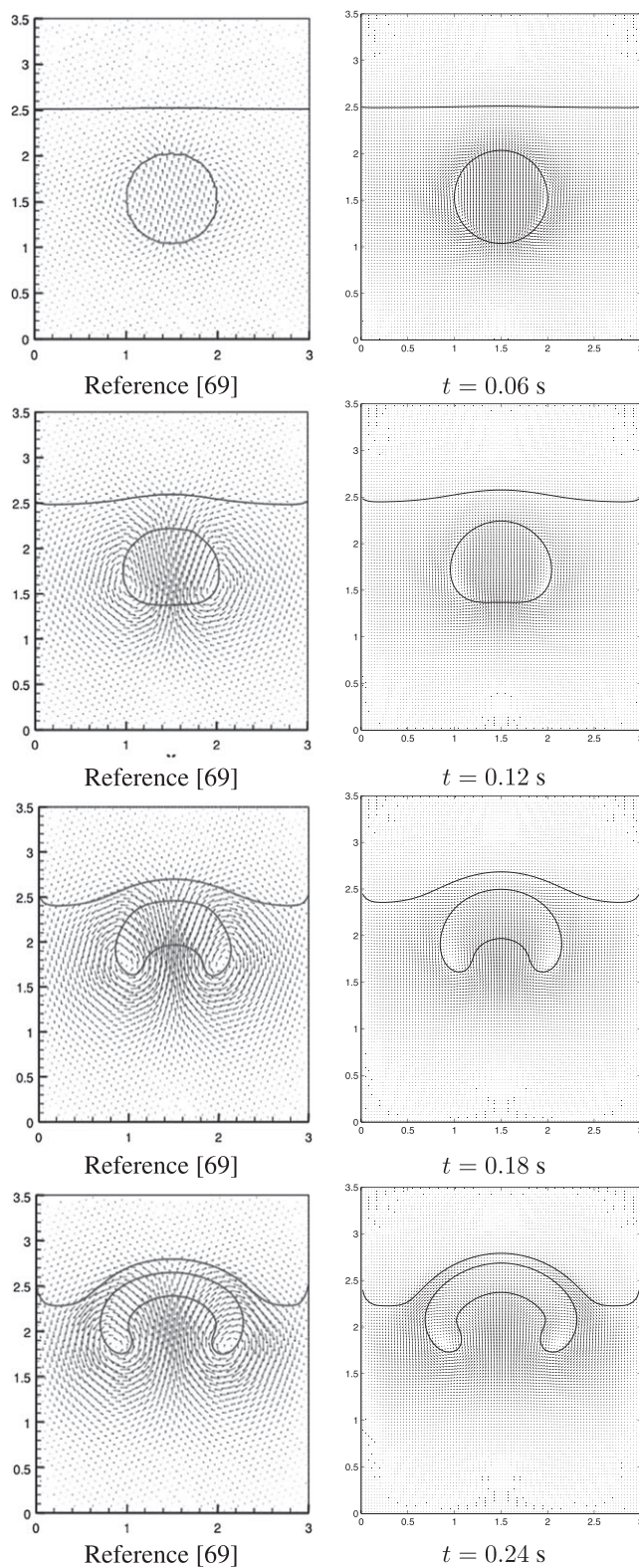


FIGURE 9 Time evolution of bubble rising inside a partially filled container. ($Re = 200$, $We = 0$). Left, reference solution.⁷¹ Right, proposed method

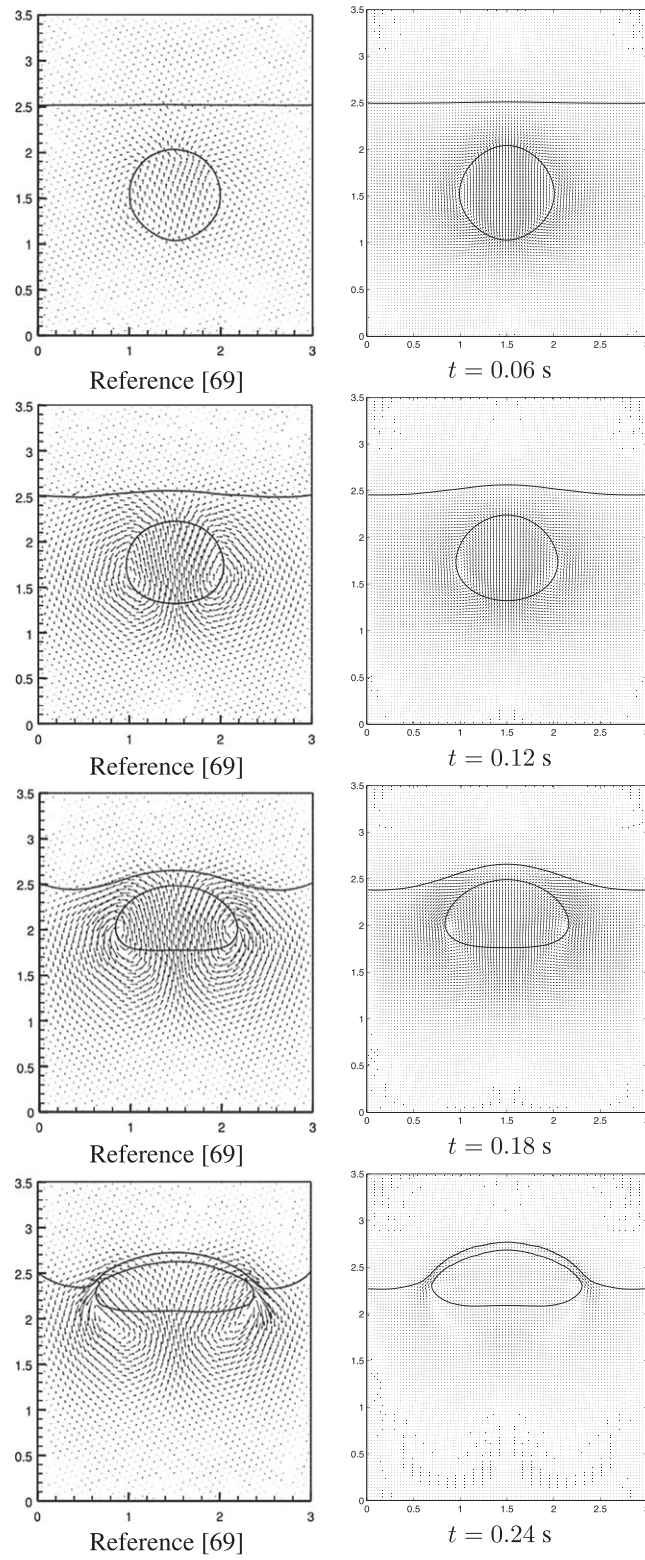


FIGURE 10 Time evolution of bubble rising in a partially filled container. ($Re = 200$, $We = 10$) Left, reference solution.⁷¹ Right, proposed method

TABLE 2 Dimensionless physical properties of the two fluids for the test case of a bubble rising in a partially filled container

Test Case 1	ρ_1/ρ_2	μ_1/μ_2	Re	We
1	1 : 2	1 : 2	200	–
2	1 : 2	1 : 2	200	10

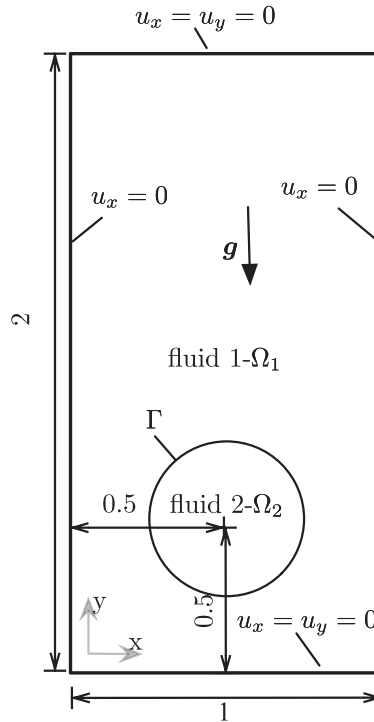


FIGURE 11 Initial configuration and boundary conditions for the problem defined in Section 5.1.3

TABLE 3 Dimensionless physical properties of the two fluids for the two test cases of a bubble rising in a fully filled container

Test Case	ρ_1	ρ_2	μ_1	μ_2	g	γ	Re	E_0	ρ_1/ρ_2	μ_1/μ_2
Case 1	1000	100	10	1	0.98	24.5	35	10	10	10
Case 2	1000	1	10	0.1	0.98	1.96	35	125	1000	100

- Circularity. The so-called “degree of circularity” of the evolving bubble can be defined as

$$C = \frac{P_a}{P_b} = \frac{\text{perimeter of the area - equivalent circle}}{\text{perimeter of the bubble}} = \frac{\pi D_a}{P_b}, \quad (45)$$

where P_a denotes the perimeter of a circular bubble with diameter D_a , which has an area equal to that of a deformed bubble with perimeter P_b . For the initial circular bubble, the circularity is equal to one and it then decreases as the deformation of the bubble increases because the initial circle encloses a larger area.

- Rising or terminal velocity defined as

$$\mathbf{u}_c = \frac{\int_{\Omega_2} \mathbf{u} \, dv}{\int_{\Omega_2} dv}. \quad (46)$$

The above is the mean velocity with which a bubble is rising or moving. This value is particularly interesting, because it measures not only the behaviour of the interface tracking algorithm but also the quality of the overall solution.

Apart from the commercial software ANSYS CFX, COMSOL, and ANSYS Fluent, 3 different open-source computer codes are compared with the proposed method, namely: (a) the TP2D (transport phenomena in 2D) code, developed in the

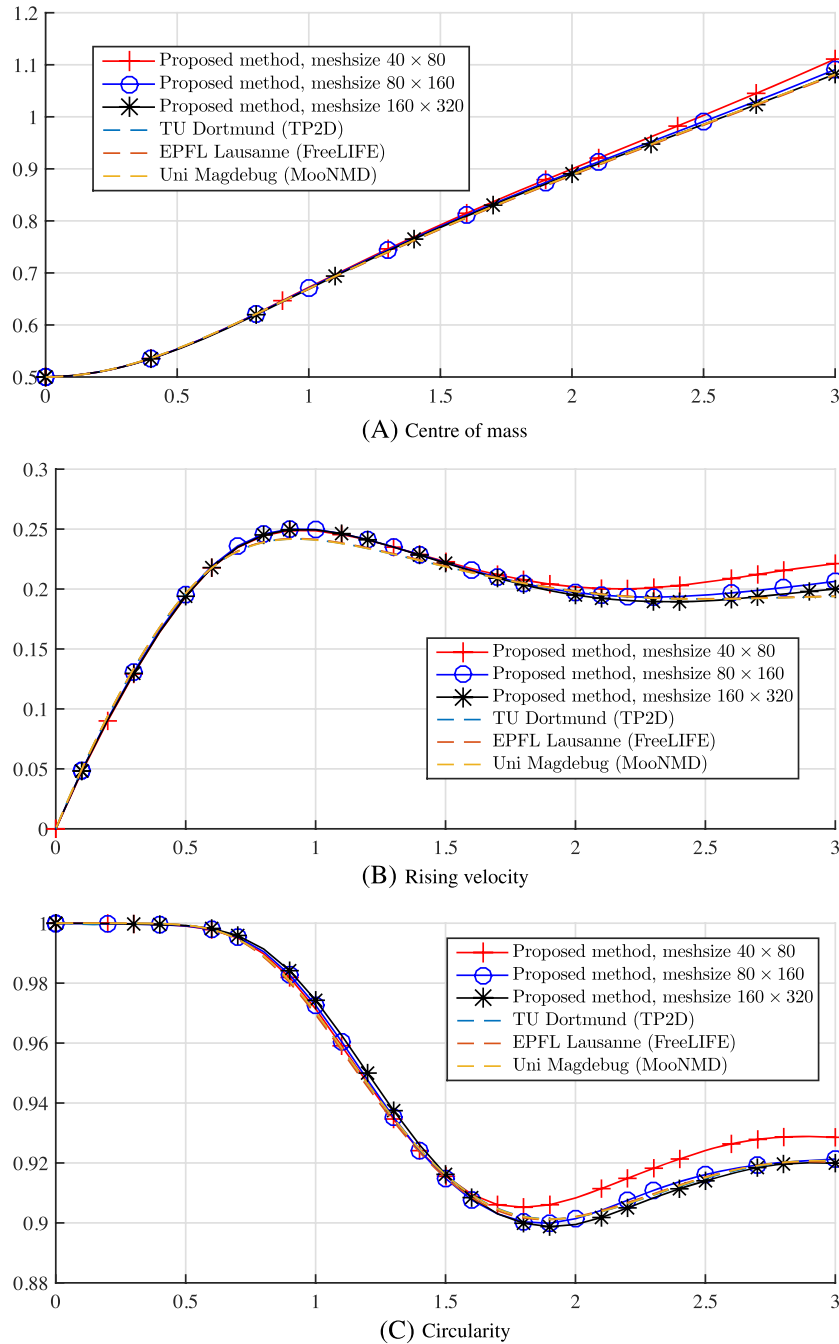
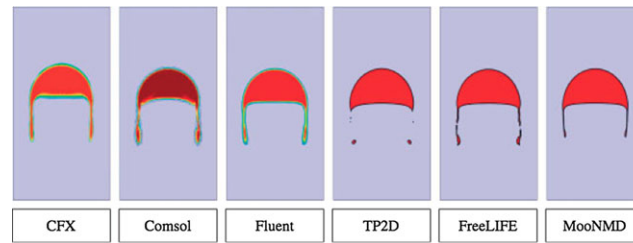


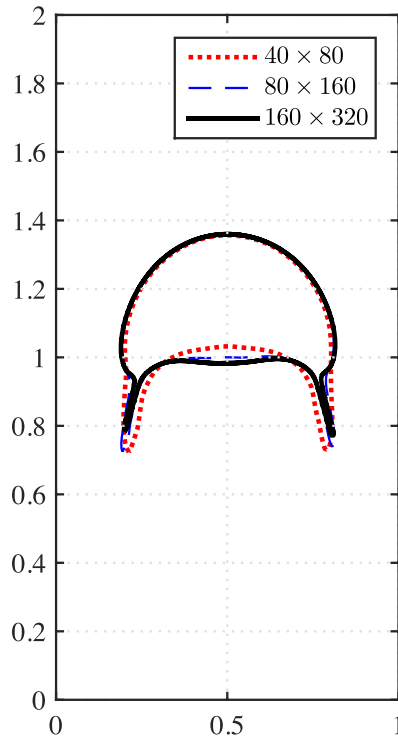
FIGURE 12 Quantitative comparison for the centre of mass, circularity, and rise velocity for the bubble rising problem of case 1. The simulation is performed with 3 levels of refinement, 40×80 , 80×160 , and 160×320 . The corresponding time refinement is as follows: $\Delta t = 3.125 \times 10^{-4}$ s, $\Delta t = 1.5625 \times 10^{-4}$ s, and $\Delta t = 7.8125 \times 10^{-5}$ s [Colour figure can be viewed at wileyonlinelibrary.com]

Technical University of Dortmund,⁷⁶ is an FEM-based incompressible flow solver,⁷⁶ combined with a level set method used to describe the interface; (b) the FreeLIFE (free-surface library of finite element) software is an FEM-based incompressible flow solver developed in EPFL Lausanne⁷⁵; and (c) the MooNMD (Mathematics and object oriented numerics in MagDeburg) is an FEM-based incompressible solver using the Arbitrary Lagrangian-Eulerian approach developed in Otto-von-Guericke University Magdeburg.⁷⁷

Case 1. The solution for test case 1 in comparison with the 3 open-source FEM-based codes (FreeLIFE, MooNMD, and TP2D) is presented in Figure 12. The bubble, being initially circular, is stretched horizontally and first develops a dimple as it rises, but after some time proceeds to assume a more stable ellipsoidal shape. No significant differences can be observed from the proposed solver and the other reference FEM solvers.



(A) Six different codes, reproduced from [73]



(B) Final shape of the rising bubble

FIGURE 13 Numerical simulation of a two-dimensional rising bubble using (A) 6 different codes and (B) proposed methodology. The simulation is performed with 3 levels of refinement: 40×80 , 80×160 , and 160×320 . The corresponding time refinement is as follows: $\Delta t = 3.125 \times 10^{-4}$ s, $\Delta t = 1.5625 \times 10^{-4}$ s, and $\Delta t = 7.8125 \times 10^{-5}$ s [Colour figure can be viewed at wileyonlinelibrary.com]

Case 2: Figure 13B shows the final shape of the bubble on a set of 3 mesh refinements. Although the bubble in both test cases rises with approximately the same speed, the decrease in surface tension causes this bubble to assume a more nonconvex shape and develop thin filaments, which might eventually break off. The benchmark results simulated using 6 different codes are taken from the work of Hysing et al⁷⁵ (see Figure 13). It can be seen that there is no agreement with respect to the thin filamentary regions. The TP2D and FreeLIFE codes show a break up of the bubble, whilst ANSYS CFX, COMSOL, ANSYS Fluent, MooNMD, and the proposed method show that the long thin trailing filaments remain intact. Figure 14 shows the quantitative comparison with other 3 softwares under mesh refinement.

5.2 | Elastic solids with multiphase flow

The aim of this section is to validate the two-phase flow solver interacting with a flexible immersed structure of very different density to that of the underlying fluid.

5.2.1 | One flapping membrane

This problem has been extracted from previous work published by Gil et al¹⁶ and will be extended to the case of different density ratios between the different phases involved. Consider an idealised two-dimensional channel $\Omega = [0, 4] \times [0, 1.61]$ filled with an incompressible Newtonian viscous fluid with viscosity $\mu = 10$ dyne/cm² s and density $\rho_f = 100$ g/cm³. A leaflet is inserted into the channel, as seen in Figure 15. The top and bottom boundaries of the channel are fixed, whereas a pulsatile nonreversible

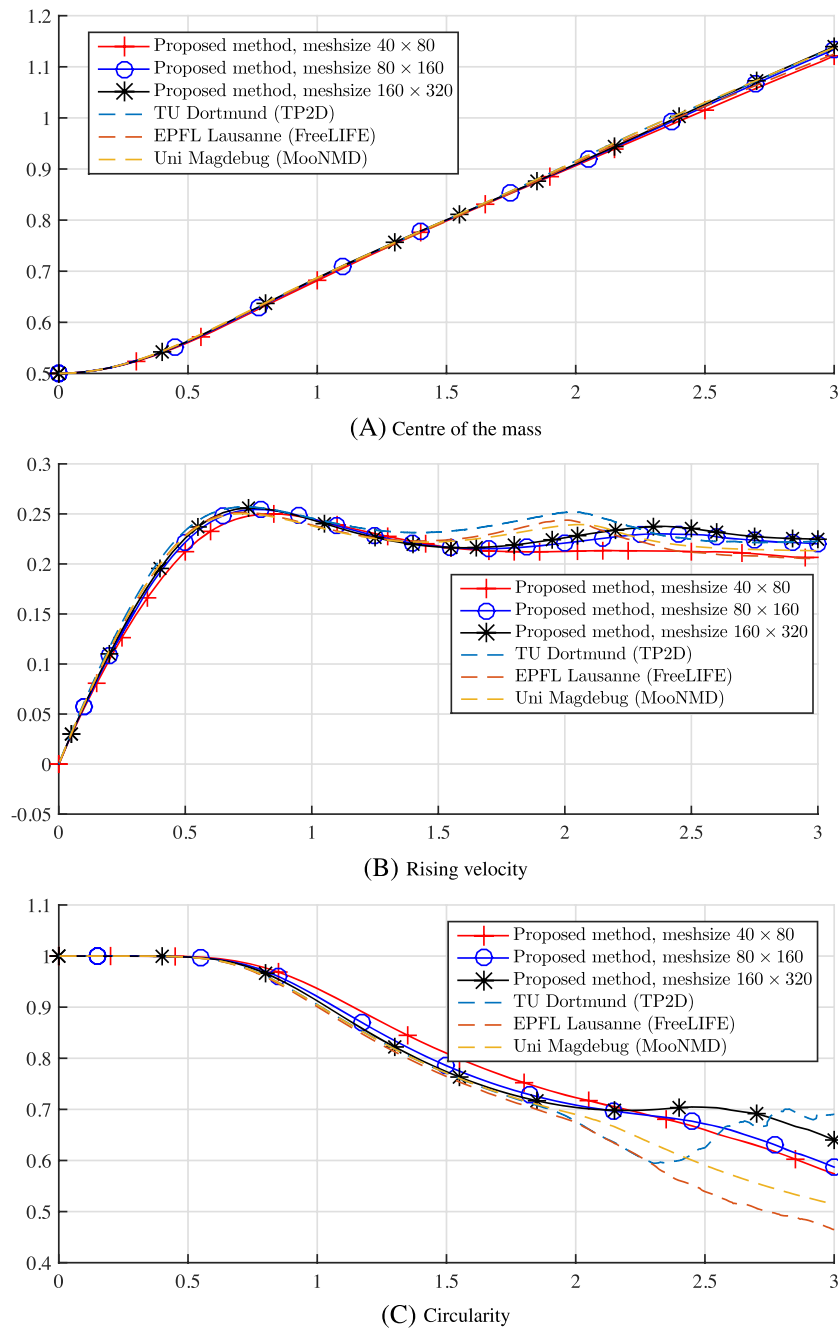


FIGURE 14 Quantitative comparison for the centre of mass, circularity, and rise velocity for the bubble rising problem of case 2. The simulation is performed with 3 levels of refinement: 40×80 , 80×160 , and 160×320 . The corresponding time refinement is as follows: $\Delta t = 3.125 \times 10^{-4}$ s, $\Delta t = 1.5625 \times 10^{-4}$ s, and $\Delta t = 7.8125 \times 10^{-5}$ s [Colour figure can be viewed at wileyonlinelibrary.com]

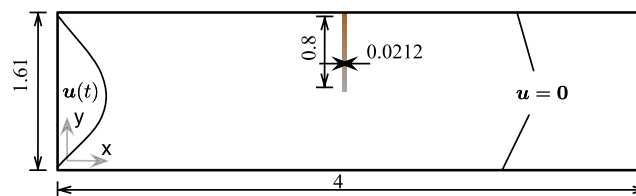


FIGURE 15 Geometry and boundary conditions for an idealised leaflet valve [Colour figure can be viewed at wileyonlinelibrary.com]

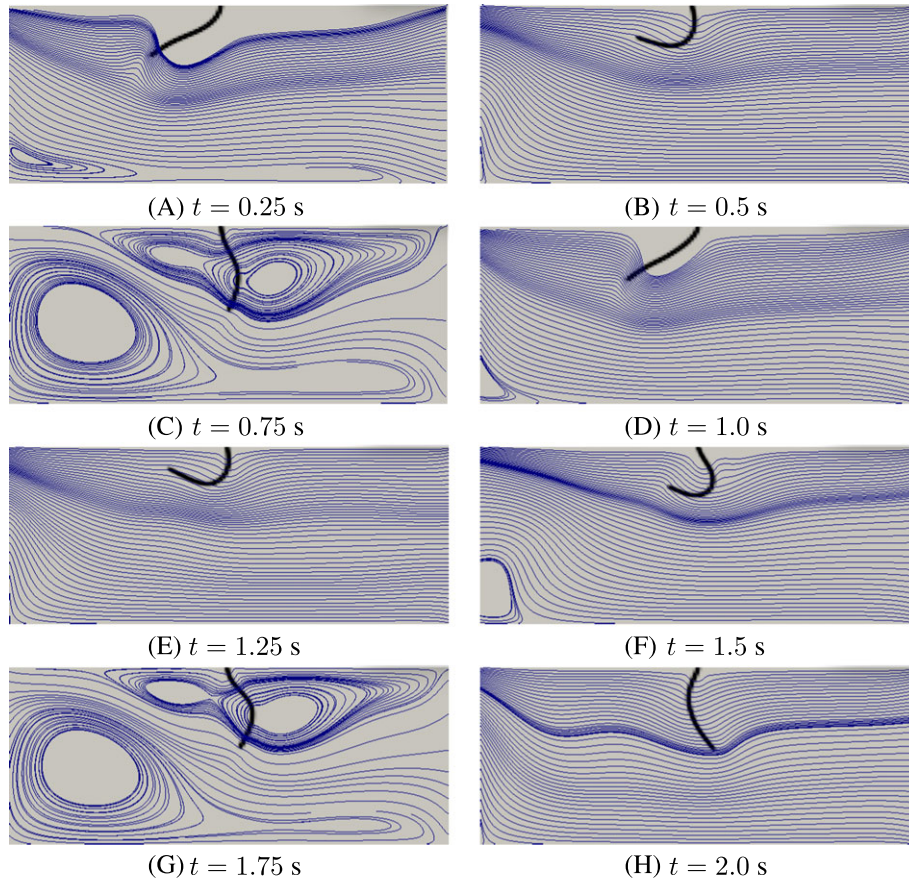


FIGURE 16 Time evolution of a flexible membrane under pulsatile flow and streamlines of the fluid. Density ratio 1 : 25, fluid viscosity $\mu = 1$ dyne/cm² s, shear modulus of $G = 2.0 \times 10^7$ dyne/cm², 4025 solid integration points, underlying fluid mesh size 160×80 , $\Delta t = 7.815 \times 10^{-4}$ s [Colour figure can be viewed at wileyonlinelibrary.com]

inflow is applied at the left boundary using a time-varying amplitude $A(t) = 5(\sin(2\pi t + 1.1))$ (the right boundary is considered to be an outflow). The leaflet is modelled using an incompressible neo-Hookean constitutive material model with shear modulus $G = 2.0 \times 10^7$ dyne/cm². This problem was analysed by Gil et al¹⁶ for a leaflet density identical to that of the underlying fluid, which is a typical situation in biomedical applications. However, here we will consider 3 test cases with different structure densities of value $\rho_s = 100, 500, 2500$ g/cm³. The objective is to observe the different leaflet dynamics and flow patterns that emerge as a result of this variation in density ratio, namely, $\rho_s/\rho_f = 1, 5, 25$ (for the case where $\rho_s/\rho_f = 1$, results were already reported by Gil et al¹⁶).

For all simulations, the underlying fluid is discretised using a 160×80 mesh, whereas 4025 integration points are used for the solid membrane. Regarding the time step discretisation, a single time step was used for all the simulations, namely, $\Delta t = 7.815 \times 10^{-4}$ s.

Figure 16 shows the time evolution of both the pulsatile flow and the deformation of the membrane for the case where $\rho_s/\rho_f = 25$. It is clear that these results differ dramatically, both in terms of flow leaflet dynamics and flow patterns, with respect to those reported in previous works^{14,16} where a density ratio $\rho_s/\rho_f = 1$ was used. Figure 17 shows the x - and y - components of the top flap tip position for the membrane for the 3 test cases. It is interesting to observe the important differences registered as the density ratio changes from 5 to 25. It can be clearly seen that the method is able to successfully model the inclusion of highly deformable structures into the fluid with a large density ratio. The methodology avoids the need to resort to a prohibitively expensive mesh moving/remeshing algorithm yet displays a robust treatment of the immersed structure.

5.2.2 | Dam break with elastic obstacle

A water column of width $a = 14.6$ cm and height $2a$ is placed in the left corner of a rectangular tank of size $4a \times 2.5a$. A geometrical representation of the problem is presented in Figure 18. The density and viscosity of the water are taken as $\rho_w = 1.0$ g/cm³, $\mu_w = 10^{-2}$ Pa s and the density and viscosity of the surrounding air $\rho_a = 1.0 \times 10^{-3}$ g/cm³, $\mu_a = 10^{-5}$ Pa s.

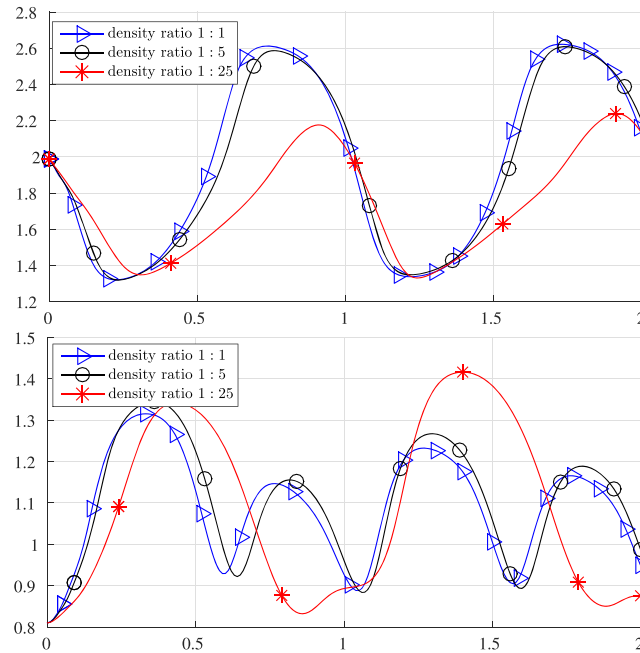


FIGURE 17 *x*- and *y*- components of the bottom left point of the membrane with different density ratio 1 : 1, 1 : 5, and 1 : 25. Fluid viscosity $\mu = 1 \text{ dyne/cm}^2 \text{ s}$, shear modulus of $G = 2.0 \times 10^7 \text{ dyne/cm}^2$, 4025 solid integration points, and mesh size 160×80 , $\Delta t = 7.815 \times 10^{-4} \text{ s}$ [Colour figure can be viewed at wileyonlinelibrary.com]

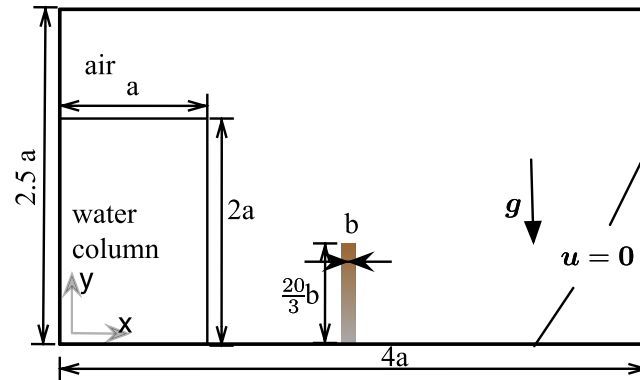


FIGURE 18 Schematics of the dam break problem interacting with an elastic obstacle [Colour figure can be viewed at wileyonlinelibrary.com]

A rectangular incompressible obstacle in the shape of a column of width $b = 1.2 \text{ cm}$, height $\frac{20}{3}b$, Young modulus $E = 10^7 \text{ g/cm/s}^2$ and $\rho_s = 2.5 \text{ g/cm}^2$ is fixed at the centre bottom of the tank. The water column is left to freely move as a result of the gravity effect and the objective of the problem is to simulate the interaction between the two-phase flow (eg, air and water) and the immersed deformable structure. As there are no experimental results available for this particular problem, the proposed methodology will be benchmarked against a variety of alternative numerical schemes available in the literature. Specifically, the same problem has been analysed with a free surface model by using a monolithic FSI method,⁷⁸ a partitioned FSI method,⁷⁹ the particle FEM,⁸⁰ and the SPH method.⁸¹

The time history of the displacement of the obstacle at the upper left corner is depicted and compared in Figure 19 by using the various methodologies. In addition, results are displayed for the proposed method by using a fluid mesh refinement study, with meshes of 64×40 , 128×80 and 256×160 . The corresponding time refinement is as follows: $\Delta t = 1.25 \times 10^{-5} \text{ s}$, $\Delta t = 6.25 \times 10^{-6} \text{ s}$, and $\Delta t = 3.125 \times 10^{-6} \text{ s}$. The elastic obstacle is modelled by using 245, 1032, and 4025 integration points, respectively. Results agree well with the different approaches.⁸⁰

The time history of the problem is displayed in Figures 20 and 21, where the fluid streamlines and vorticity contours are also shown. These figures are obtained for the finest mesh. As it can be seen, when the water column hits the obstacle, the left upper

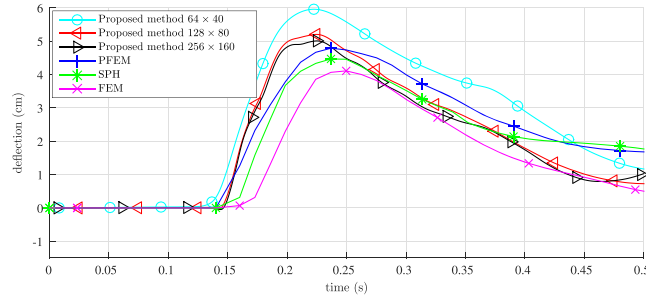


FIGURE 19 Dam break with elastic obstacle: history of the x -displacement of the upper left corner of the obstacle. The corresponding time refinement is as follows: $\Delta t = 1.25 \times 10^{-5} s$, $\Delta t = 6.25 \times 10^{-6} s$, and $\Delta t = 3.125 \times 10^{-6} s$ [Colour figure can be viewed at wileyonlinelibrary.com]

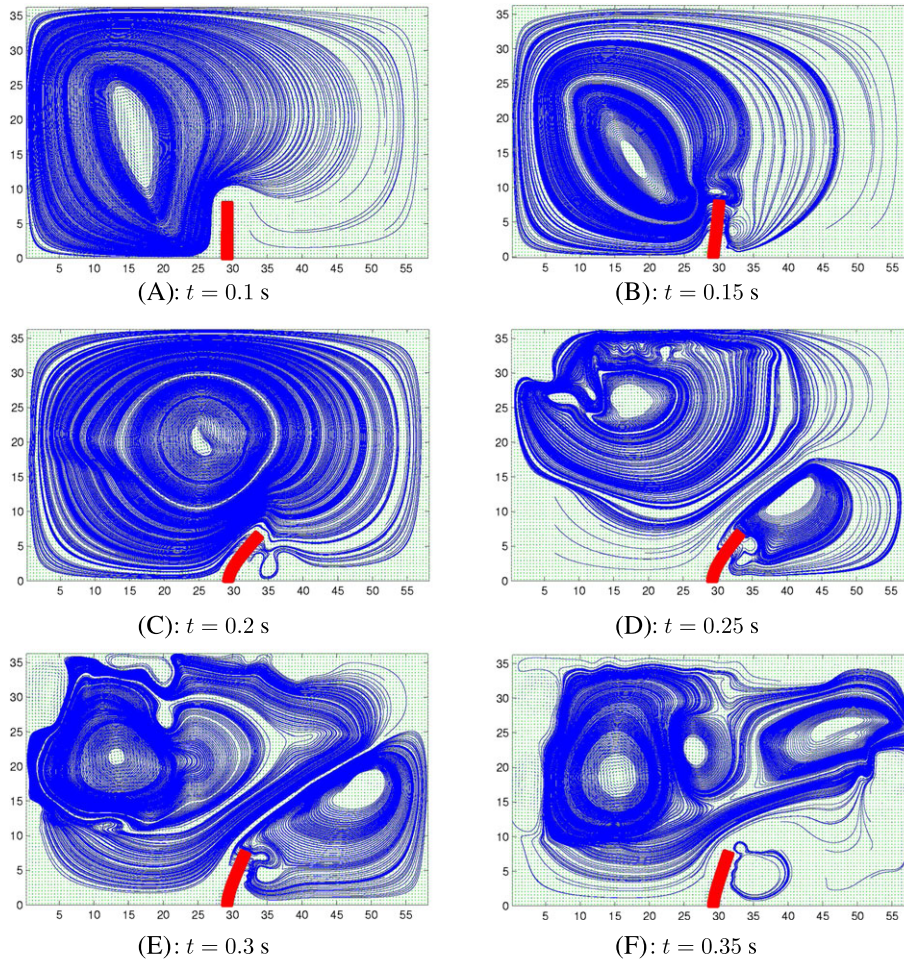


FIGURE 20 Dam break with elastic obstacle: time history and streamlines of the fluid. Water density $\rho_w = 1.0 \text{ g/cm}^3$, air density $\rho_a = 1.0 \times 10^{-3} \text{ g/cm}^3$, structure density $\rho_s = 2.5 \text{ g/cm}^3$, water viscosity $\mu_w = 10^{-2} \text{ dyne/cm}^2 \text{ s}$, air viscosity $\mu_a = 10^{-5} \text{ dyne/cm}^2 \text{ s}$, Young modulus $E = 10^7 \text{ g/cm/s}^2$, mesh size 256×160 , 4025 integration points [Colour figure can be viewed at wileyonlinelibrary.com]

corner first deflects to the left, and whilst the water level rises, it progressively moves to the right. The maximum deflection is obtained at around $t = 0.2 \text{ s}$ when the water passes the top of the obstacle and is fully attached to the left side of the structure. As it is expected, the impact of the water column against the elastic obstacle causes the latter to oscillate.

5.2.3 | Elastic wall under time-dependent water pressure effects

This problem was first presented by Antoci et al.⁸² The problem consists of an elastic gate, clamped at its top end, and free at its bottom end, which interacts with a mass of water initially confined in a free-surface tank behind the gate. Figure 22 shows a

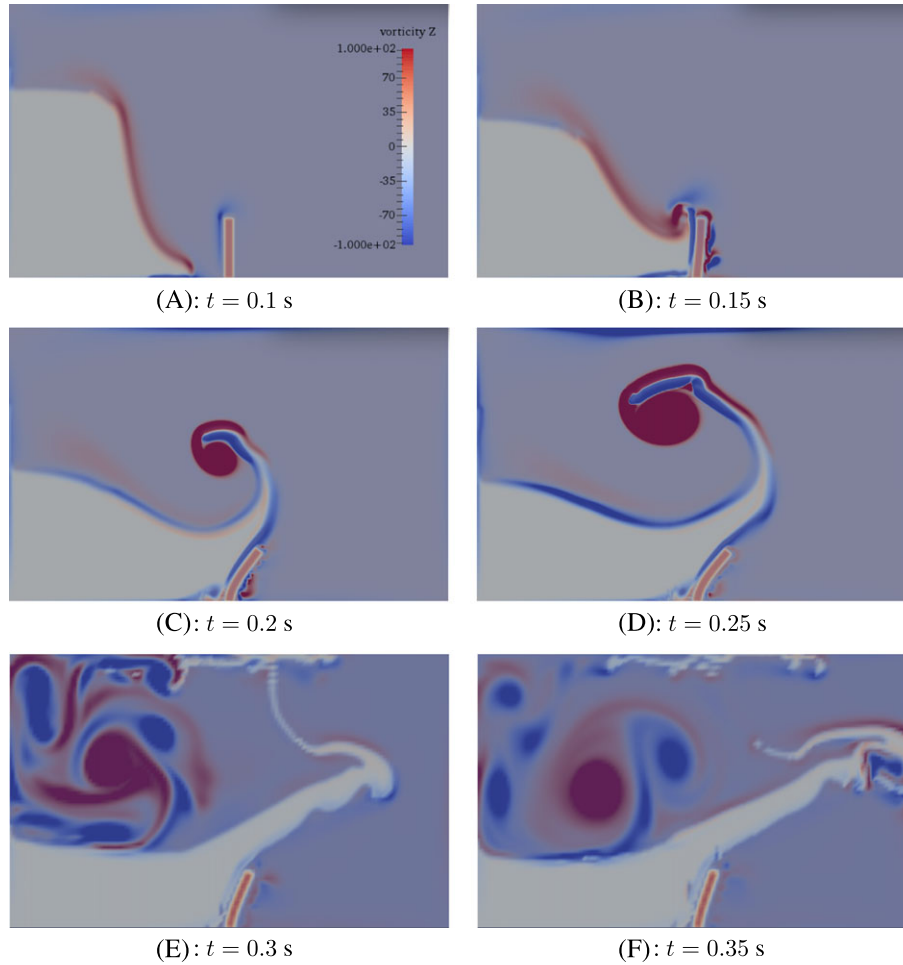


FIGURE 21 Dam break with elastic obstacle: time evolution and vorticity contours of the fluid, vorticity contours ($-100 < \omega < 100$). Water density $\rho_w = 1.0 \text{ g/cm}^3$, air density $\rho_a = 1.0 \times 10^{-3} \text{ g/cm}^3$, structure density $\rho_s = 2.5 \text{ g/cm}^3$, water viscosity $\mu_w = 10^{-2} \text{ dyne/cm}^2 \text{ s}$, air viscosity $\mu_a = 10^{-5} \text{ dyne/cm}^2 \text{ s}$, Young's modulus $E = 10^7 \text{ g/cm/s}^2$, mesh size 256×160 , 4025 integration points [Colour figure can be viewed at wileyonlinelibrary.com]

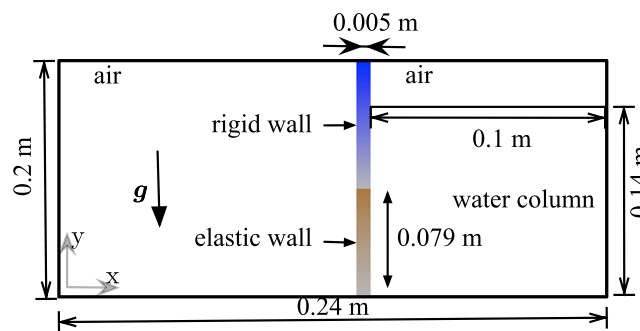


FIGURE 22 Schematics of the tank with immersed elastic gate [Colour figure can be viewed at wileyonlinelibrary.com]

geometrical representation of the problem. The flexible gate, 5-mm thick, is made of rubber with a density of 1100 kg/m^3 and a constant 10 MPa Young modulus.

The simulation is performed by using a mesh of 288×160 cells with the elastic gate modelled by means of 4025 integration points. The time step used for the simulation was $\Delta t = 3.125 \times 10^{-6} \text{ s}$. Figure 23 displays the time history of the number of fixed-point iterations (for a tolerance of 10^{-6} in the relative norm). As it can be observed, an average value of 4 fixed-point iterations is depicted per time step. In all the numerical examples presented in this paper, similar behaviour was observed. This is the same approach adopted in former works.^{13,16}

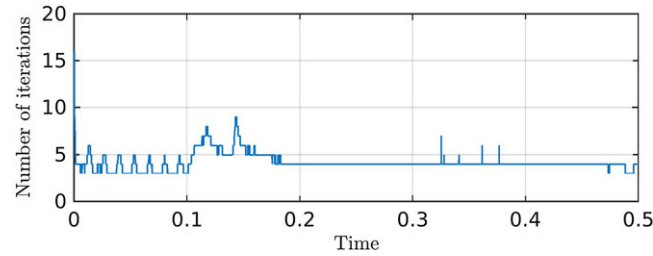


FIGURE 23 Time history of the number of fixed-point iterations per time step [Colour figure can be viewed at wileyonlinelibrary.com]

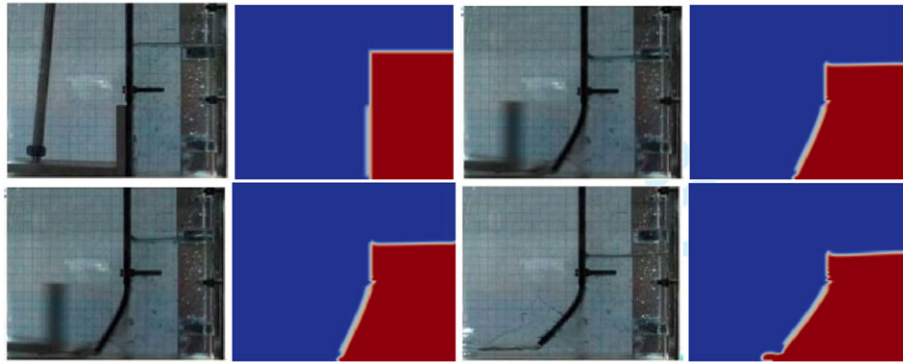


FIGURE 24 Comparison of numerical and experimental results every 0.08 s. Water density $\rho_w = 1.0 \times 10^3 \text{ kg/m}^3$, air density $\rho_a = 1.0 \text{ kg/m}^3$, structure density $\rho_s = 1.1 \times 10^3 \text{ kg/m}^3$, water viscosity $\mu_w = 10^{-3} \text{ Pa s}$, air viscosity $\mu_a = 10^{-5} \text{ Pa s}$, Young modulus $E = 10 \text{ MPa}$, mesh size 288×160 , 4025 integration points for the solid [Colour figure can be viewed at wileyonlinelibrary.com]

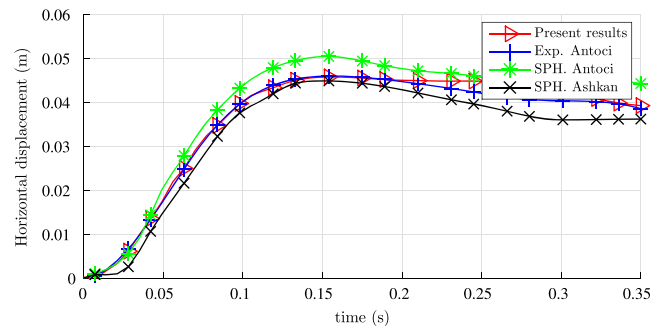


FIGURE 25 Comparison of the horizontal displacement of the free end of the gate. Water density $\rho_w = 1.0 \times 10^3 \text{ kg/m}^3$, air density $\rho_a = 1.0 \text{ kg/m}^3$, structure density $\rho_s = 1.1 \times 10^3 \text{ kg/m}^3$, water viscosity $\mu_w = 10^{-3} \text{ Pa s}$, air viscosity $\mu_a = 10^{-5} \text{ Pa s}$, Young's modulus $E = 10 \text{ MPa}$, mesh size 288×160 , 4025 integration points for the solid [Colour figure can be viewed at wileyonlinelibrary.com]

Comparison of a time sequence of snapshots between the numerical solutions obtained from the proposed algorithm and the experimental results reported by Antoci et al⁸² is illustrated in Figure 24.

The problem was also simulated numerically in the work of Antoci et al⁸² by using the SPH method. For comparison purposes between the different schemes, Figure 25 shows the time evolution of the horizontal displacement at the free end of the flexible gate. It is clear that the maximum deformation occurs near the free end of the gate, showing excellent agreement with the experimental results provided by Antoci et al,⁸² outperforming the results obtained with the SPH approach. The gate reaches its maximum deformation at time $t = 0.15 \text{ s}$, after which the difference between the various techniques increases because of the higher complexity of the physics of the problem and the various modelling simplifying assumptions introduced.

6 | CONCLUSIONS

This paper presents a unified “one-fluid” computational framework for the numerical analysis of two-dimensional multiphase incompressible FSI problems in the context of hydrodynamics. The proposed method builds on the existing immersed structural

potential method developed by Gil et al^{13,16} to overcome the restriction of having to deal with similar density ratios among different phases or the restriction to solve single-phase flows. For the description of the various phases, a smooth representation of the sharp indicator function is used, in conjunction with the level set method for the capturing of the fluid-fluid interfaces and an interface Lagrangian-based meshless technique for the tracking of the fluid-structure interface. The modelling of fluid and solid phases only differs in the definition of the deviatoric contribution to the Cauchy stress tensor. In terms of applicability and reliability, a wide range of benchmark and applications have been presented in the numerical examples, including bubble dynamics, hydrodynamics, and FSI with free surfaces. These problems are assessed to prove the robustness and flexibility of the proposed computational methodology. Extension of this framework to a 3-dimensional parallelised version in conjunction with a more efficient Runge-Kutta-based coupled time integrator along with a complete Eulerian description of the deformable solid via an extended set of conservation laws are the next steps of our work.

ACKNOWLEDGEMENTS

The first author acknowledges the financial support received through “The Zienkiewicz Scholarship” awarded by College of Engineering, Swansea University. The second and fourth authors gratefully acknowledge the financial support provided by the Sêr Cymru National Research Network for Advanced Engineering and Materials, United Kingdom. The second author would also like to acknowledge the financial support received through “The Leverhulme Prize” awarded by The Leverhulme Trust, United Kingdom.

ORCID

Liang Yang  <http://orcid.org/0000-0003-0901-0929>

Antonio J. Gil  <http://orcid.org/0000-0001-7753-1414>

REFERENCES

1. Sarrate J, Huerta A, Donea J. Arbitrary Lagrangian-Eulerian formulation for fluid-rigid body interactions. *Comput Methods Appl Mech Eng*. 2001;190(24-25):3171-3188.
2. Dettmer W, Peric D. A computational framework for fluid-rigid body interaction: finite element formulation and applications. *Comput Methods Appl Mech Eng*. 2006;195(13-16):1633-1666.
3. Wood C, Gil AJ, Hassan O, Bonet J. Partitioned block-Gauss-Seidel coupling for dynamic fluid-structure interactions. *Comput Struct*. 2010;88(23):1367-1382.
4. Badia S, Nobile F, Vergara C. Fluid-structure partitioned procedures based on Robin transmission conditions. *J Comput Phys*. 2008;227(14):7027-7051.
5. Badia S, Quaini A, Quarteroni A. Splitting methods based on algebraic factorization for fluid-structure interaction. *SIAM J Sci Comput*. 2008;30(4):1778-1805.
6. Peskin CS. Flow patterns around heart valves: a numerical method. *J Comput Phys*. 1972;10(2):252-271.
7. Peskin CS. Numerical analysis of blood flow in the heart. *J Comput Phys*. 1977;25(3):220-252.
8. Peskin CS, McQueen DM. Modeling prosthetic heart valves for numerical analysis of blood flow in the heart. *J Comput Phys*. 1980;37(1):113-132.
9. Peskin CS, McQueen DM. A three-dimensional computational method for blood flow in the heart I. Immersed elastic fibers in a viscous incompressible fluids. *J Comput Phys*. 1989;81(2):372-405.
10. Lim S, Peskin CS. Fluid-mechanical interaction of flexible bacterial flagella by the immersed boundary method. *Phys Rev E*. 2012;85(3):036307.
11. Liu WK, Liu Y, Farrell D, et al. Immersed finite element method and its applications to biological systems. *Comput Methods Appl Mech Eng*. 2006;195(13):1722-1749.
12. Zhang L, Gerstenberger A, Wang X, Liu WK. Immersed finite element methods. *Comput Methods Appl Mech Eng*. 2004;193(21):2051-2067.
13. Gil AJ, Arranz Carreño A, Bonet J, Hassan O. An enhanced immersed structural potential method for fluid-structure interactions. *J Comput Phys*. 2013;250(0):178-205.
14. Hesch C, Gil AJ, Arranz Carreño A, Bonet J. On continuum immersed strategies for fluid structure interaction. *Comput Methods Appl Mech Eng*. 2012;247-248(0):51-64.
15. Hesch C, Gil AJ, Arranz Carreño A, Bonet J, Betsch P. A mortar approach for fluid-structure interaction problems: immersed strategies for deformable and rigid bodies. *Comput Methods Appl Mech Eng*. 2014;278:853-882.
16. Gil AJ, Arranz Carreño A, Bonet J, Hassan O. The immersed structural potential method for haemodynamic applications. *J Comput Phys*. 2010;229(22):8613-8641.
17. Gerstenberger A, Wall WA. An extended finite element method/Lagrange multiplier based approach for fluid structure interaction. *Comput Methods Appl Mech Eng*. 2008;197:1699-1714.
18. Alauzet F, Fabrèges B, Fernández MA, Landajuela M. Nitsche-XFEM for the coupling of an incompressible fluid with immersed thin-walled structures. *Comput Methods Appl Mech Eng*. 2016;301:300-335.

19. Burman E, Fernández MA. An unfitted Nitsche method for incompressible fluid-structure interaction using overlapping meshes. *Comput Methods Appl Mech Eng*. 2014;279:497-514.
20. McQueen DM, Peskin CS. A three-dimensional computational method for blood flow in the heart. II. Contractile fibers. *J Comput Phys*. 1989;82(2):289-297.
21. Peskin CS. The immersed boundary method. *Acta Numerica*. 2002;11:479-517.
22. Devendran D, Peskin CS. An immersed boundary energy-based method for incompressible viscoelasticity. *J Comput Phys*. 2012;231(14):4613-4642.
23. Kim Y, Peskin CS. Numerical study of incompressible fluid dynamics with nonuniform density by the immersed boundary method. *Phys Fluids*. 2008;20(6):062101.
24. Kim Y, Lai MC, Peskin CS. Numerical simulations of two-dimensional foam by the immersed boundary method. *J Comput Phys*. 2010;229(13):5194-5207.
25. Griffith BE, Hornung RD, McQueen DM, Peskin CS. An adaptive, formally second order accurate version of the immersed boundary methods. *J Comput Phys*. 2007;223(1):10-49.
26. Wang X, Liu WK. Extended immersed boundary method using FEM and RKPM. *Comput Methods Appl Mech Eng*. 2004;193(12-14):1305-1321.
27. Zhang L, Gerstenberger A, Wang X, Liu WK. Immersed finite element method. *Comput Methods Appl Mech Eng*. 2004;193(21-22):2051-2067.
28. Sulsky D, Kaul A. Implicit dynamics in the material-point method. *Comput Methods Appl Mech Eng*. 2004;193(12):1137-1170.
29. Zhao H, Freund JB, Moser RD. A fixed-mesh method for incompressible flow-structure systems with finite solid deformations. *J Comput Phys*. 2008;227(6):3114-3140.
30. Lee CH, Gil AJ, Bonet J. Development of a cell centred upwind finite volume algorithm for a new conservation law formulation in structural dynamics. *Comput Struct*. 2013;118:13-38.
31. Lee CH, Gil AJ, Bonet J. Development of a stabilised Petrov-Galerkin formulation for conservation laws in Lagrangian fast solid dynamics. *Comput Methods Appl Mech Eng*. 2014;268:40-64.
32. Karim IA, Lee CH, Gil AJ, Bonet J. A two-step Taylor-Galerkin formulation for fast dynamics. *Eng Comput*. 2014;31(3):366-387.
33. Gil AJ, Lee CH, Bonet J, Aguirre M. A stabilised Petrov-Galerkin formulation for linear tetrahedral elements in compressible, nearly incompressible and truly incompressible fast dynamics. *Comput Methods Appl Mech Eng*. 2014;276:659-690.
34. Bonet J, Gil AJ, Lee CH, Aguirre M, Ortigosa R. A first order hyperbolic framework for large strain computational solid dynamics. Part I: total Lagrangian isothermal elasticity. *Comput Methods Appl Mech Eng*. 2015;283:689-732.
35. Gil AJ, Lee CH, Bonet J, Ortigosa R. A first order hyperbolic framework for large strain computational solid dynamics – Part II: Total Lagrangian compressible, nearly incompressible and truly incompressible elasticity. *Comput methods Appl Mech Eng*. 2016;300: 146-181.
36. Aguirre M, Gil AJ, Bonet J, Arranz Carreño A. A vertex centred finite volume Jameson-Schmidt-Turkel (JST) algorithm for a mixed conservation formulation in solid dynamics. *J Comput Phys*. 2014;259:672-699.
37. Ren B, Li C, Yan X, Lin MC, Bonet J, Hu SM. Multiple-fluid SPH simulation using a mixture model. *ACM Trans Graphics (TOG)*. 2014;33(5):171.
38. Balachandar S, Eaton JK. Turbulent dispersed multiphase flow. *Annu Rev Fluid Mech*. 2010;42:111-133.
39. Unverdi SO, Tryggvason G. A front-tracking method for viscous, incompressible, multi-fluid flows. *J Comput Phys*. 1992;100(1):25-37.
40. Popinet S, Zaleski S. A front-tracking algorithm for accurate representation of surface tension. *Int J Numer Methods Fluids*. 1999;30(6): 775-793.
41. Tryggvason G, Bunner B, Esmaeeli A, et al. A front-tracking method for the computations of multiphase flow. *J Comput Phys*. 2001;169(2):708-759.
42. Brackbill J, Kothe D, Zemach C. A continuum method for modeling surface tension. *J Comput Phys*. 1992;100(2):335-354.
43. Lafaurie B, Nardone C, Scardovelli R, Zaleski S, Zanetti G. Modelling merging and fragmentation in multiphase flows with SURFER. *J Comput Phys*. 1994;113(1):134-147.
44. Sethian JA. A fast marching level set method for monotonically advancing fronts. *Proc. Natl. Acad. Sci*. 1996;93:1591-1595.
45. Legay A, Chesa J, Belytschko T. An Eulerian-Lagrangian method for fluid – structure interaction based on level sets. *Comput Methods Appl Mech Eng*. 2006;195:2070-2087.
46. Franci A, Oñate E, Carbonell JM. Unified Lagrangian formulation for solid and fluid mechanics and FSI problems. *Comput Methods Appl Mech Eng*. 2016;298:520-547.
47. Bonet J, Gil AJ, Ortigosa R. A computational framework for polyconvex large strain elasticity. *Comput Methods Appl Mech Eng*. 2015;283:1061-1094.
48. Bonet J, Gil AJ, Wood RD. *Nonlinear Solid Mechanics for Finite Element Analysis: Statics*. Cambridge, UK:Cambridge University Press; 2016.
49. Gil AJ, Ortigosa R. A new framework for large strain electromechanics based on convex multi-variable strain energies: variational formulation and material characterisation. *Comput Methods Appl Mech Eng*. 2016;302:293-328.
50. Toro EF. *Riemann Solvers and Numerical Methods for Fluid Dynamics: A Practical Introduction*. New York:Springer Science & Business Media; 2013.
51. Lee CH, Gil AJ, Bonet J. Development of a cell centred upwind finite volume algorithm for a new conservation law formulation in structural dynamics. *Comput Struct*. 2013;118(0):13-38.
52. Aguirre M, Gil AJ, Bonet J, Lee CH. An upwind vertex centred finite volume solver for Lagrangian solid dynamics. *J Comput Phys*. 2015;300:387-422.
53. Marsden JE, Hughes TJR. *Mathematical foundations of elasticity*. Dover Publications, New York: 1994.

54. Prosperetti A, Tryggvason G. *Computational Methods for Multiphase Flows*. Cambridge, UK: Cambridge University Press; 2007.
55. Osher S, Sethian J. Fronts propagating with curvature-dependent speed: algorithms based on Hamilton-Jacobi formulations. *J Comput Phys*. 1988;79(1):12-49.
56. Sussman M, Smereka P, Osher S. A level set approach for computing solutions to incompressible two-phase flow. *J Comput Phys*. 1994;114(1):146-159.
57. Yang L. An Immersed Computational Framework for Multiphase Fluid-Structure Interaction (Doctoral dissertation). Swansea University, 2015.
58. Yang L, Carreno AA, Gil AJ, Bonet J. An Immersed Structural Potential Method framework for incompressible flexible/rigid/multi-phase flow interactions. In Proc. 22nd UK Conference of the Association for Computational Mechanics in Engineering Exeter:UK; 2014.
59. Boffi D, Gastaldi L, Heltai L, Peskin CS. On the hyper-elastic formulation of the immersed boundary methods. *Comput Methods Appl Mech Eng*. 2008;197(25):2210-2231.
60. Yang L, Badia S, Codina R. A pseudo-compressible variational multiscale solver for turbulent incompressible flows. *Computational mechanics*. 2016;58(6):1051-1069.
61. Harlow FH, Welch JE. Numerical calculation of time-dependent viscous incompressible flow of fluid with free surface. *Phys Fluids*. 1965;8(12):2182-2189.
62. Gaskell PH, Lau AKC. Curvature-compensated convective transport: SMART, a new boundedness-preserving transport algorithms. *Int J Numer Methods Fluids*. 1988;8(6):617-641.
63. Zhu J. A low-diffusive and oscillation-free convection scheme. *Commun Appl Numer Methods*. 1991;7(3):225-232.
64. Leonard BP. A stable and accurate convective modelling procedure based on quadratic upstream interpolation. *Comput Methods Appl Mech Eng*. 1979;19(1):59-98.
65. Kim J, Moin P. Application of a fractional-step method to incompressible Navier-Stokes equations. *J Comput Phys*. 1985;59(2):308-323.
66. Wang X, Liu WK. Extended immersed boundary method using FEM and RKPM. *Comput Methods Appl Mech Eng*. 2004;193(12):1305-1321.
67. Bardenhagen S, Brackbill J, Sulsky D. The material-point method for granular materials. *Comput Methods Appl Mech Eng*. 2000;187(3):529-541.
68. Falgout RD, Yang UM. Hypre: a library of high performance preconditioners. In: International Conference on Computational Science. Amsterdam, The Netherlands: Springer; 2002:632-641.
69. Martin JC, Moyce WJ. An experimental study of the collapse of liquid columns on a rigid horizontal plane. *Philos Trans R Soc London. Ser A, Math Phys Sci*. 1952;244(1):312-324.
70. Hu C, Sueyoshi M. Numerical simulation and experiment on dam break problem. *J Mar Sci Appl*. 2010;9(2):109-114.
71. Zhao Y, Tan HH, Zhang B. A high-resolution characteristics-based implicit dual time-stepping VOF method for free surface flow simulation on unstructured grids. *J Comput Phys*. 2002;183(1):233-273.
72. Kelecy FJ, Pletcher RH. The development of a free surface capturing approach for multidimensional free surface flows in closed containers. *J Comput Phys*. 1997;138(2):939-980.
73. Xia J, Lin B, Falconer RA, Wang G. Modelling dam-break flows over mobile beds using a 2D coupled approach. *Adv Water Resour*. 2010;33(2):171-183.
74. Sheu TWH, Yu CH, Chiu PH. Development of a dispersively accurate conservative level set scheme for capturing interface in two-phase flows. *J Comput Phys*. 2009;228(3):661-686.
75. Hysing S, Turek S, Kuzmin D, et al. Quantitative benchmark computations of two-dimensional bubble dynamics. *Int J Numer Methods Fluids*. 2009;60(11):1259-1288.
76. Turek S, Becker C. FEATFLOW Finite element software for the incompressible Navier-Stokes equations, User Manual Release 1.1. *Preprint, Heidelberg*. 1998;4.
77. John V, Matthies G. MoonMMD—a program package based on mapped finite element methods. *Comput Visualization Sci*. 2004;6(2-3):163-170.
78. Walhorn E, Kölke A, Hübner B, Dinkler D. Fluid-structure coupling within a monolithic model involving free surface flows. *Comput Struct*. 2005;83(25-26):2100-2111.
79. Kassiotis C, Ibrahimbegovic A, Matthies H. Partitioned solution to fluid-structure interaction problem in application to free-surface flows. *Eur J Mech-B/Fluids*. 2010;29(6):510-521.
80. Idelsohn SR, Marti J, Limache A, Oñate E. Unified Lagrangian formulation for elastic solids and incompressible fluids: application to fluid structure interaction problems via the PFEM. *Comput Methods Appl Mech Eng*. 2008;197(19-20):1762-1776.
81. Rafiee A, Thiagarajan KP. An SPH projection method for simulating fluid-hypoelastic structure interaction. *Comput Methods Appl Mech Eng*. 2009;198(33-36):2785-2795.
82. Antoci C, Gallati M, Sibilla S. Numerical simulation of fluid-structure interaction by SPH. *Comput Struct*. 2007;85(11-14):879-890. Fourth MIT Conference on Computational Fluid and Solid Mechanics.
83. Burman Erik, Hansbo Peter. Fictitious domain finite element methods using cut elements: I. A stabilized Lagrange multiplier method. *Comput Methods Appl Mech Eng*. 2010;199:2680-2686.

How to cite this article: Yang L, Gil AJ, Carreño AA, Bonet J. Unified one-fluid formulation for incompressible flexible solids and multiphase flows: Application to hydrodynamics using the immersed structural potential method (ISPM). *Int J Numer Meth Fluids*. 2017;1–29. <https://doi.org/10.1002/flid.4408>